



**HAL**  
open science

# Linker gadolinium as charge channel and singlet oxygen activation site in graphitic carbon nitride for enhancing photocatalytic decomposition of tetracycline

Jianmin Luo, Wenqin Li, Xinglei Wang, Eric Lichtfouse, Donglan Huang,  
Xiaoyuan Chen, Yi Zhang, Lejie Zhu, Chuanyi Wang

## ► To cite this version:

Jianmin Luo, Wenqin Li, Xinglei Wang, Eric Lichtfouse, Donglan Huang, et al.. Linker gadolinium as charge channel and singlet oxygen activation site in graphitic carbon nitride for enhancing photocatalytic decomposition of tetracycline. *Journal of Rare Earths*, 2024, 42 (5), pp.827-837. 10.1016/j.jre.2024.02.008 . hal-04677279

**HAL Id: hal-04677279**

**<https://hal.science/hal-04677279v1>**

Submitted on 26 Aug 2024

**HAL** is a multi-disciplinary open access archive for the deposit and dissemination of scientific research documents, whether they are published or not. The documents may come from teaching and research institutions in France or abroad, or from public or private research centers.

L'archive ouverte pluridisciplinaire **HAL**, est destinée au dépôt et à la diffusion de documents scientifiques de niveau recherche, publiés ou non, émanant des établissements d'enseignement et de recherche français ou étrangers, des laboratoires publics ou privés.

Public Domain

# Linker gadolinium as charge channel and singlet oxygen activation site in graphitic carbon nitride for enhancing photocatalytic decomposition of tetracycline<sup>☆</sup>

Jianmin Luo<sup>a, b, c, \*</sup>, Wenqin Li<sup>a, c</sup>, Xinglei Wang<sup>b</sup>, Eric Lichtfouse<sup>d</sup>, Donglan Huang<sup>a</sup>, Xiaoyuan Chen<sup>a</sup>, Yi Zhang<sup>a</sup>, Lejie Zhu<sup>a, \*\*, \*\*\*</sup>, Chuanyi Wang<sup>e, \*\*\*\*</sup>

<sup>a</sup> College of Chemistry and Civil Engineering, Shaoguan University, Shaoguan, 512005, China

<sup>b</sup> Key Laboratory of Pollutant Chemistry and Environmental Treatment, College of Chemistry and Environmental Science, Yili Normal University, Yining, 835000, China

<sup>c</sup> College of Chemistry and Environmental Science, Kashi University, Kashi, 844006, China

<sup>d</sup> CNRS, IRD, INRAE, Coll France, CEREGE, Aix-Marseille University, Aix en Provence, 13100, France

<sup>e</sup> Guangzhou Institute of Industrial Intelligence (GIII), Guangzhou, 511400, China

## A B S T R A C T

Reactive oxygen species are essential in photocatalytic water treatment. In this paper, Gd doped carbon nitride (CN) photocatalysts were prepared by simple thermal polymerization for the photocatalytic degradation of tetracycline under visible light irradiation. The photodegradation rate of 1.0GdCN is as high as 95% in 18 min, and the photocatalytic performance is much higher than that of CN. The improvement of photocatalytic performance is mainly attributed to the fact that Gd ion implantation directly provides active sites for oxygen activation and induces the formation of N vacancies. The results of characterizations show that the introduction of Gd in CN can improve the conversion ability of activated oxygen, carrier separation and energy band structure adjustment. Therefore, 1.0GdCN photocatalyst can be employed for efficient photocatalytic synthesis of tetracycline. Furthermore, three ways of photocatalytic degradation of tetracycline were revealed by high performance liquid chromatography-mass spectrometry. This work provides insights into the doping strategy of CN to improve the production of reactive oxygen species for environmental remediation.

## Keywords:

Photocatalysis  
Tetracycline  
Hydrogen peroxide  
Gd doped CN  
Singlet oxygen  
Rare earths

\* Corresponding author. School of Chemistry and Civil Engineering, Shaoguan University, Shaoguan, 512005, China.

\*\* Corresponding author.

\*\*\* Corresponding author.

E-mail addresses: [xyyljm@163.com](mailto:xyyljm@163.com) (J. Luo), [229015878@qq.com](mailto:229015878@qq.com) (L. Zhu), [wangchuanyi@sust.edu.cn](mailto:wangchuanyi@sust.edu.cn) (C. Wang).

## 1. Introduction

Photocatalysis technology based on semiconductors is expected to solve the problem of water environment pollution.<sup>1–3</sup> Unfortunately, the photocatalytic mineralization efficiency of organic pollutants is still relatively low.<sup>4–6</sup> The essence of photocatalytic reaction is a chain reaction between reactive oxygen species (ROSS) and organic pollutants. Obtaining high quality ROSSs is the key to the efficiency of photocatalysis improvement.<sup>7–10</sup> The common ROSSs (<sup>1</sup>O<sub>2</sub>, •O<sub>2</sub><sup>-</sup>, H<sub>2</sub>O<sub>2</sub> and •OH) play an irreplaceable role in photocatalysis.<sup>11–14</sup> Many photocatalysts have been widely used to catalyze the reduction of two-electron oxygen to H<sub>2</sub>O<sub>2</sub>.<sup>15–17</sup> In particular, carbon nitride (CN) has become a popular material because of its merits such as metal-free, light response, suitable band structure and unique physical and chemical properties.<sup>18–20</sup> However, the rapid recombination of electron–hole pairs and exposed active sites limit the photoactivity of the original CN.<sup>21–23</sup>

Various strategies have been used to modify pristine CN, such as metal/nonmetal doping, morphology modulation, noble metal loading, defect engineering, hybridization and constructing heterojunctions.<sup>24–26</sup> Among them, defect engineering is a common and effective method to obtain CNs with excellent performance.<sup>27–29</sup> The introduction of structural defects can not only tune the optical and electrical properties of CN, but also overcome the kinetic barrier in the oxygen reduction process, thus enabling the effective construction of impurity bands on the CN surface.<sup>30–32</sup> Nevertheless, the following issues have not been paid attention to: (1) in the design of carbon nitride with structural defects, the stacking of  $\pi$ - $\pi$  layers has been neglected, which makes the charge transfer from bulk to surface difficult; (2) in the photocatalytic  $O_2$  reduction reaction, reshaping defects to enhance the binding strength with  $O_2$  may be more critical than simply exposing more defects; (3) Some measures are needed to overcome the reverse recombination behavior of surface electrons.<sup>33–38</sup> Therefore, obtaining CN with functional defects on the surface and dense  $\pi$ - $\pi$  layer stacking in the bulk phase is a work worthy of exploration and challenge.<sup>39–42</sup>

In the past few years, many modification methods, such as metal or non-metal doped, molecular copolymerization, and the construction of heterojunctions, have been developed to improve the photocatalytic performance of CN.<sup>43–45</sup> As rare earth elements, lanthanides showed great potential as doped agents.<sup>46–48</sup> For example, Luo's research group<sup>13</sup> employed Ce to modify CN, and the as-obtained Ce-doped CN exhibited excellent photocatalytic activity. Because Gd and Ce possess very close valence layer electrons, both 4p and 4f orbitals interact with the  $\pi$ - $\pi$  bond of CN, so it is inferred that Gd doped CN could show good oxygen adsorption and activation ability for oxygen.

In this study, 1.0GdCN photocatalysts were prepared using lanthanide Gd and thermal polymerization of melamine. Optimized 1.0GdCN showed excellent photocatalytic degradation of tetracycline (TC) under visible light irradiation. Based on characterizations and theoretical calculations, the improved photocatalytic performance of 1.0GdCN may be attributed to better oxidation ability and electrical conductivity than pure CN. Moreover, the introduction of Gd elements and the formation of N vacancies inhibited the rapid recombination of photogenerated electron–hole pairs and provided active sites for activating oxygen. Finally, 1.0GdCN exhibited an enhanced generation of ROSs ( $^1O_2$  and  $\bullet OH$ ) for photocatalytic degradation of TC. This work revealed a Gd doping strategy to improve the generation of ROSs for water treatment.

## 2. Experimental

### 2.1. Materials

Gadolinium acetate and melamine came from Macklin. All chemicals were of analytical reagent grade or higher and were used without further purification.

### 2.2. Synthesis of the catalysts

Typically, 4 g of melamine and different amounts of gadolinium acetate (0.020, 0.0320, 0.040, 0.050 and 0.060 g) were put into 100 mL boiling water and stirred for 40 min using a magnetic stirrer and placed in a dry oven until the water solution had dried. Then, it was thermally treated in a muffle furnace at a heating rate of 4 °C/min and kept for 5 h at 550 °C. Finally, the resulting sol was dried and ground, obtaining a light-yellow powder of Gd-g- $C_3N_4$ , denoted as GdCN. According to the proportion of gadolinium acetate to melamine, the samples were labeled as 0.5GdCN, 0.8GdCN,

1.0GdCN, 1.2GdCN and 1.5GdCN, respectively. The different proportions of Gd doped CN were fabricated through a thermal polymerization method.

As a reference, pure g- $C_3N_4$  was also synthesized, where melamine was put in a ceramic pot and heated at 550 °C for 5 h in a muffle furnace. Then the sample was cooled in the oven to room temperature. The bulk sample was ground to obtain the pale-yellow g- $C_3N_4$  powder, denoted as CN.

### 2.3. Catalysts characterization

The parameters of the test and characterization processes are detailed in Text S1 of SI.

### 2.4. Photoactive evaluation

The degradation efficiency of TC was used as the index to measure the photocatalytic performance of the samples. The visible light source was a 300 W xenon lamp (PLS-SXE300/300 UV), using a glass filter to remove the ultraviolet light with a wavelength below 420 nm. Typically, 100 mg of the photocatalyst was added to a 100 mL solution containing 10 mg/L TC and stirred for 30 min under dark conditions to achieve an adsorption–desorption equilibrium. Under visible light irradiation, 2 mL of the mixture was sampled at intervals of 3 min. The TC solution and the photocatalyst were separated by a 0.22  $\mu m$  filter membrane. The concentration of the TC aqueous solution was measured by high-performance liquid chromatography (HPLC, Shimadzu) with an EC-C18 column (4.6 mm  $\times$  150 mm). The column temperature was set to be 25 °C, and the detection wavelength was 280 nm. The ratio of 0.3% aqueous phosphoric acid solution to methanol in the mobile phase was 6:4, and the flow rate was 1 mL/min. The sample volume was 20  $\mu L$  for each injection. The formula for calculating the photocatalytic degradation efficiency ( $A$ ) of TC was as follows:

$$A = c_0 - \frac{c_t}{c_0} \times 100\% \quad (1)$$

where  $c_0$  represents the initial TC concentration, while  $c_t$  represents the TC concentration after  $t$  min of photodegradation.

### 2.5. Photoelectrochemical experiment

The parameters of the test and characterization processes are detailed in Text S2 of SI.

### 2.6. Active species trapping experiments

The parameters of the test and characterization processes are detailed in Text S3 of SI.

### 2.7. Theoretical calculations

The parameters of the test and characterization processes are detailed in Text S4 of SI.

## 3. Results and discussion

### 3.1. Morphology and structure analysis

As shown in Fig. 1(a), Gd-doped CN photocatalysts were prepared by simple thermal polycondensation at 550 °C. In order to determine the surface morphology and possible elements of

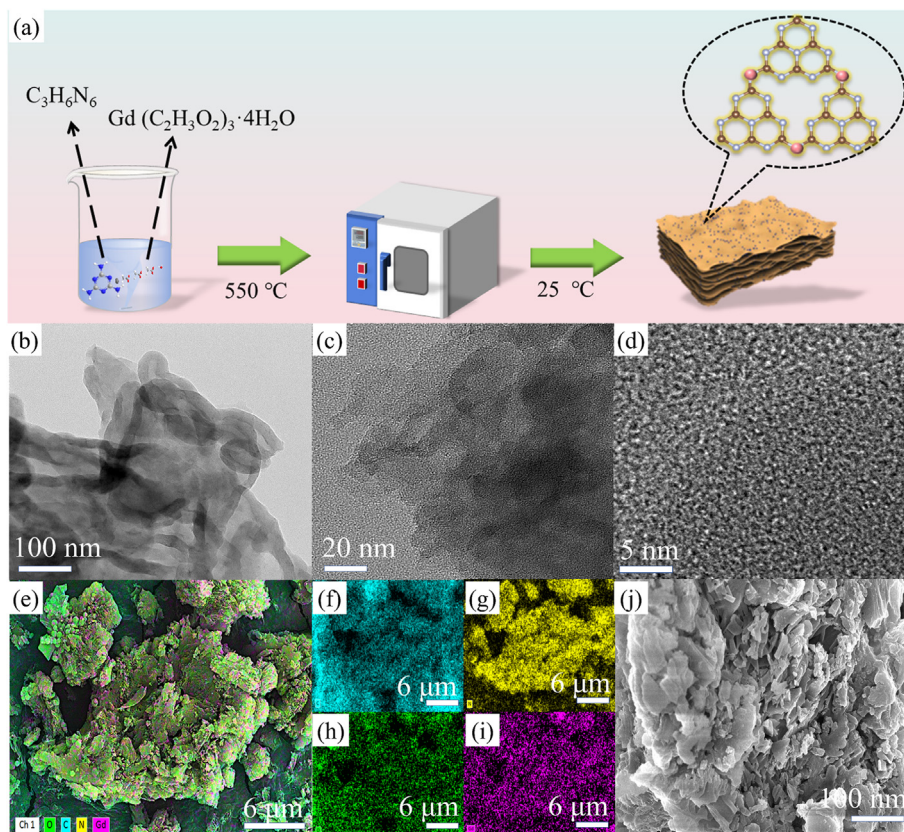


**Fig. 1.** (a) Illustration of the synthetic process employed in producing 1.0GdCN; (b–d) TEM images of 1.0GdCN; SEM mapping images of 1.0GdCN (e), C (f), N (g), O (h) and Gd (i); (j) SEM image of 1.0GdCN.

photocatalysts 1.0GdCN and CN, the scanning electron microscope (SEM, XFlash 6130 sigma500) and transmission electron microscope (TEM, FEI talos f200s) were used. As can be seen from Fig. 1(b–d) and Fig. S1, 1.0GdCN shows an irregular shape. As shown in Fig. S2, the CN sample shows an amorphous morphology consistent with that of 1.0GdCN. In addition, in order to further verify the elemental composition of 1.0GdCN, EDS analysis and elemental mapping patterns were carried out (Fig. 1(e–i) and Fig. S3). Among them, Gd, C, N and O elements are uniformly distributed on the surface of 1.0GdCN, which indicates that Gd element has been successfully injected into CN. It is worth noting that, combined with Fig. 1(j) and Fig. S2, both 1.0GdCN and CN show a massive structure, which may be due to the result of *in-situ* thermal polymerization.

Large specific surface area and rich pore structure provide more active centers for photocatalytic reaction, so it can improve the removal efficiency of photocatalysis. Fig. S4 and Table S1 show that the specific surface area of 1.0GdCN is 13.3 m<sup>2</sup>/g, which is much larger than that of CN 8.6 m<sup>2</sup>/g. In addition, the porous properties of 1.0GdCN also changed after doping, as described by Barrett–Joyner–Helena (BJH) methods. The pore size distribution shows that the volume of 1.0GdCN is obviously larger than that of CN, but the pore size of 1.0GdCN is smaller than that of CN. To sum up, the injection of Gd element increases the degree of polymerization of 1.0GdCN, which leads to a larger specific surface area. It can be concluded that the doping of Gd has significant effect on the specific surface area of CN. Therefore, the improvement of photocatalytic activity of CN by Gd doping may be related to the increase of its specific surface area.

### 3.2. Chemical compositions

The X-ray diffraction patterns of the crystal structures of different samples are shown in Fig. S5, 1.0GdCN samples show characteristic peaks at 13.2° and 27.4°, corresponding to (100) and (002) crystal planes, respectively, representing triazine ring structure and layer spacing, which are also characteristic peaks of pure CN.<sup>49</sup> The above results show that the peak intensity of 1.0GdCN photocatalyst samples and other photocatalysts with different ratios do not change much after Gd doping, which may be due to the low amount of Gd doped. To reveal the chemical molecular structures of CN and GdCN, FT-IR measurements were carried out. As shown in Fig. S6, CN and GdCN have obvious peaks at approximately 810, 1200, 1750, 3000 and 3400 cm<sup>-1</sup>. The peak around 810 cm<sup>-1</sup> represents the out-of-plane bending mode of the triazine units. The peaks at 1200–1750 cm<sup>-1</sup> and 3000–3400 cm<sup>-1</sup> correspond to the stretching vibrations mode of C–N heterocycles and N–H in bridged or terminal amine groups, respectively.<sup>46</sup> These findings are consistent with the results of XRD patterns. In addition, we found that Gd-doped photocatalysts adsorbed more H<sub>2</sub>O than CN, especially 1.0GdCN. The 1.0GdCN and CN samples showed the same peak positions, demonstrating that the presence of the Gd element did not change the basic framework of CN.

The chemical properties of 1.0GdCN and CN were characterized in detail by X-ray photoelectron spectroscopy (XPS). As shown in Fig. 2(a), only C, N and O are found in the measured spectra of 1.0GdCN, which is consistent with the powder CN. Among them, there is no characteristic peak of Gd in energy spectrum, which may be caused by the low content of Gd. Fig. 2(b) shows the C 1s XPS fine spectrum of 1.0GdCN and CN, respectively. There are two peaks in

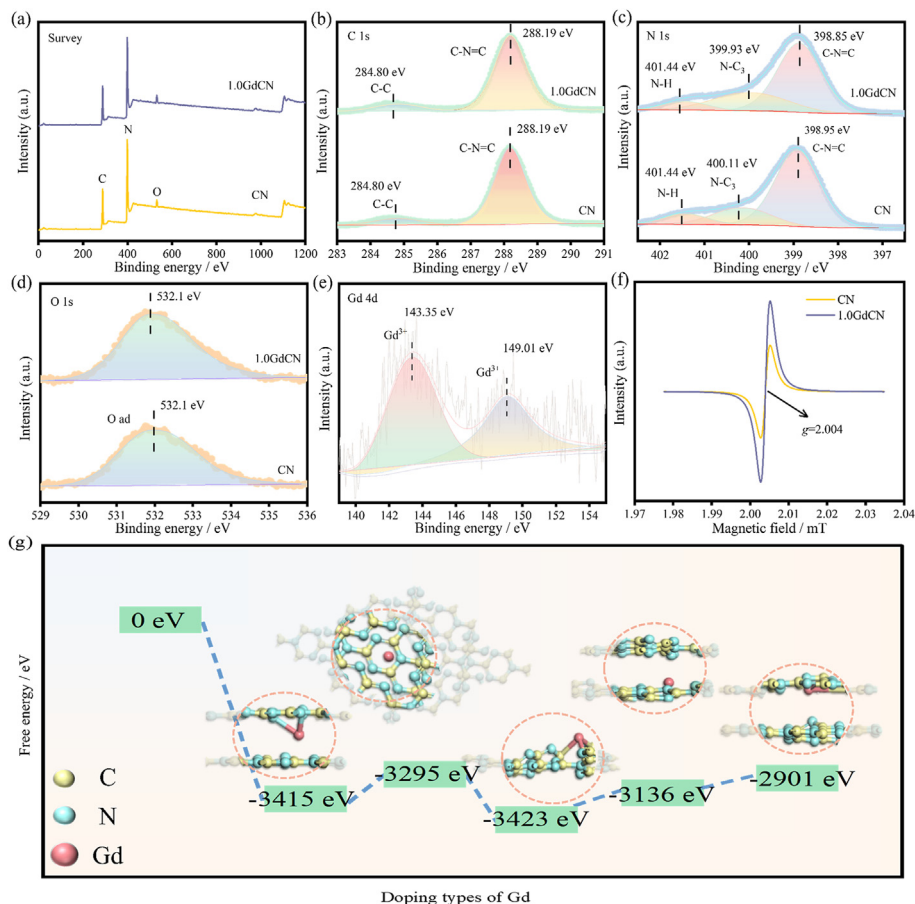


**Fig. 2.** XPS spectra for CN and 1.0GdCN: survey spectra (a), C 1s (b), N 1s (c), O 1s (d) and Gd 4d (e); (f) EPR of N vacancy; (g) Heat absorption and release of various possible structures in DFT calculation.

1.0GdCN and CN. The peak at 284.8 eV<sup>26,50</sup> belongs to C–C and the peak at 288.19 eV<sup>51</sup> belongs to  $sp^2$  hybrid C–N=C. Fig. 2(c) depicts the high-resolution XPS spectrum of N 1s of 1.0GdCN and CN. Among them, the peaks of 1.0GdCN are 401.44, 399.93 and 398.85 eV, which represent the  $sp^2$  bond nitrogen in N–aromatic ring (C–N–C), tertiary nitrogen group N–(C)<sub>3</sub> and amino group (C–N–H), respectively. However, compared with the N 1s fine spectrum peak of CN (401.44, 400.11 and 398.95 eV), the C=N–C peak in 1.0GdCN spectrum shifts to higher binding energy, and the bridge N peak blue shifts, indicating that there may be a chemical force between Gd and CN. At the same time, as shown in Table S2, the area of C=N–C and bridging nitrogen of 1.0GdCN decreases after fitting, indicating that N defects are mainly formed in the position of C=N–C and bridging nitrogen of 1.0GdCN. In Fig. 2(d), it is also found that the O 1s of the peaks of 1.0GdCN and CN are located at 532.10 and 532.1 eV, respectively, which are the eigenvalues of adsorbed oxygen. In the high resolution Gd 4d XPS spectrum (Fig. 2(e)), two peaks appear at 143.35 and 149.01 eV, which are attributed to  $Gd^{3+} 2p^{3/2}$  and  $Gd^{3+} 2p^{1/2}$ , respectively. To sum up, we can preliminarily infer that Gd ions are doped in the N site and produce N defects, and the electron aggregation occurs on the surface, which leads to the decrease of binding energy. It is further speculated that the injection of Gd element and the constructed 1.0GdCN photocatalyst may affect the electron transfer.

In this study, N vacancy was introduced by high temperature roasting. Due to the different stability of different bonds in 1.0GdCN molecules, high temperature calcination will lead to the fracture of some specific bonds, resulting in N atoms escaping from specific

positions and forming N vacancies. Therefore, the generation of N vacancy in the synthesis process was tested. The EPR signal due to the  $sp^2$ -carbon atoms in the p-conjugated aromatic rings generated similar unpaired electrons. Specifically, the loss of the N atom in the structure left extra electrons that were redistributed to adjacent C atoms to form additional unpaired electrons. As shown in Fig. 2(f), the EPR signal at  $g = 2.004$  of 1.0GdCN and CN, it is obvious that the signal peak of 1.0GdCN is higher than CN. After the introduction of Gd element, the amplitude of 1.0GdCN curve is larger than that of CN curve, implying a large number of defects in 1.0GdCN. Similar results are reflected in XPS data. The XPS analysis shows that the C/N ratio of CN is higher than that of 1.0GdCN, while the peak area ratio of C–N=C to N=C–N of 1.0GdCN is lower than that of CN, indicating that N mainly occurs at bridging nitrogen site (Table S2). The increase in the value of C/N and decreased peak areas also indicate that the defects generated should belong to N vacancy. It shows that the strong peak density indicates that a certain number of surface vacancies are formed on the surface of 1.0GdCN. Combined with XPS N1, the successful formation of nitrogen vacancy is fully determined.

It is well known that the free energy of lower doping sites is usually more likely to be replaced. In order to clarify the doping position of Gd element in CN, we calculated the single-point energy levels of different energy levels at different positions on the surface of 1.0GdCN. As shown in Fig. 2(g) and Table S3, the Gd ion replaces the C, Gd ion is in the cavity of the azine ring structure, the Gd substitutes bridged N, Gd exists at the interlayer site, and Gd substitutes for triazine N. These free energies are

respectively:  $-3415$ ,  $-329$ ,  $-3423$ ,  $-3136$  and  $-2901$  eV. The final calculation results show that the energy of Gd substituting bridging nitrogen sites is the lowest, and only  $-3423$  eV is needed. Therefore, it has the greatest potential to replace the bridging nitrogen position. It shows that Gd has successfully replaced this position, which is consistent with our above XPS results.

### 3.3. Optical properties

Then the optical properties of the photocatalyst were studied. Firstly, the solid UV diffuse reflection was used to test the photocatalyst. As shown in Figs. 3(a) and 1.0GdCN appears as an obvious absorption edge in the 450 nm region, while CN is only near 420 nm. It is worth noting that the absorption band and light capture ability of the modified 1.0GdCN photocatalyst are significantly improved, and there is a signal between 500 and 600 nm. In addition, other photocatalysts with different ratios have different degrees of absorption edge redshift. Therefore, it can further show that the response of the modified composite samples to visible light is enhanced. In addition, 1.0GdCN showed the strongest absorption in the UV–visible region.

The band gap energy of photocatalyst was calculated by Kubelka–Munk function. As shown in Fig. 3(b), the bandgap width of 1.0GdCN is 2.64 eV, while that of CN is 2.78 eV. Because the band gap of 1.0GdCN is smaller than that of CN, it shows better response to visible light. As shown in Fig. 3(c, d), according to the valence band X-ray photoelectron spectroscopy (VB-XPS) data, the VB potential ( $E_{VB}$ ) values of 1.0GdCN and CN are 1.99 and 2.22 eV, respectively. Therefore, the  $E_{VB, XPS}$  can be evaluated according to the VB-XPS method. Then, the  $E_{VB}$  of the corresponding standard hydrogen electrode ( $E_{VB, NHE}$ ) can be calculated according to the following formula:

$$E_{VB, NHE} \equiv \varphi + E_{VB, XPS} + 4.44 \quad (2)$$

where  $\varphi$  is the work function of the instrument (4.63 eV). Thus, the  $E_{VB, NHE}$  of 1.0GdCN and CN was calculated to be 2.18 and 2.41 eV. Then, according to  $E_{VB}$  and  $E_g$ , the conduction band potential ( $E_{CB}$ ) could be determined using the following equation:

$$E_{CB} = E_{VB} - E_g \quad (3)$$

From the above results, the  $E_{CB}$  of 1.0GdCN and CN are  $-0.46$  and  $-0.37$  eV, respectively. As a result, 1.0GdCN has a more negative  $E_{CB}$  than CN, which may cause 1.0GdCN to have greater reductive power.

Firstly, after understanding the optical properties of Gd-doped CN, we further studied the electronic properties of 1.0GdCN and CN. As shown in Fig. 4(a) and Fig. S7, the band gap energy of 1.0GdCN is 0.499 eV, on the contrary, the band gap energy of pure CN is 2.174 eV. Therefore, compared with CN, the band gap of 1.0GdCN is much smaller than that of CN. Therefore, it can be proved that the electron transfer ability of 1.0GdCN is improved with the introduction of Gd element. In addition, it is worth noting that through the theoretical calculation of DOS, it can be found that the energy values of conduction band and valence band of 1.0GdCN are much larger than those of CN. Therefore, with the introduction of f orbitals of Gd element, the electron energy of 1.0GdCN photocatalyst is greatly increased, which is beneficial to the separation of photogenerated carriers. It can be further shown that Gd injection affects the photocatalytic performance of 1.0GdCN.

Electrochemical impedance spectroscopy (EIS) is a common method to analyze the separation ability of photogenerated  $e^-$  and  $h^+$ . As we all know, the smaller the curve, the smaller the electrochemical impedance. As shown in Fig. 4(b), the impedance of 1.0GdCN is much smaller than that of CN. According to Table S4, the

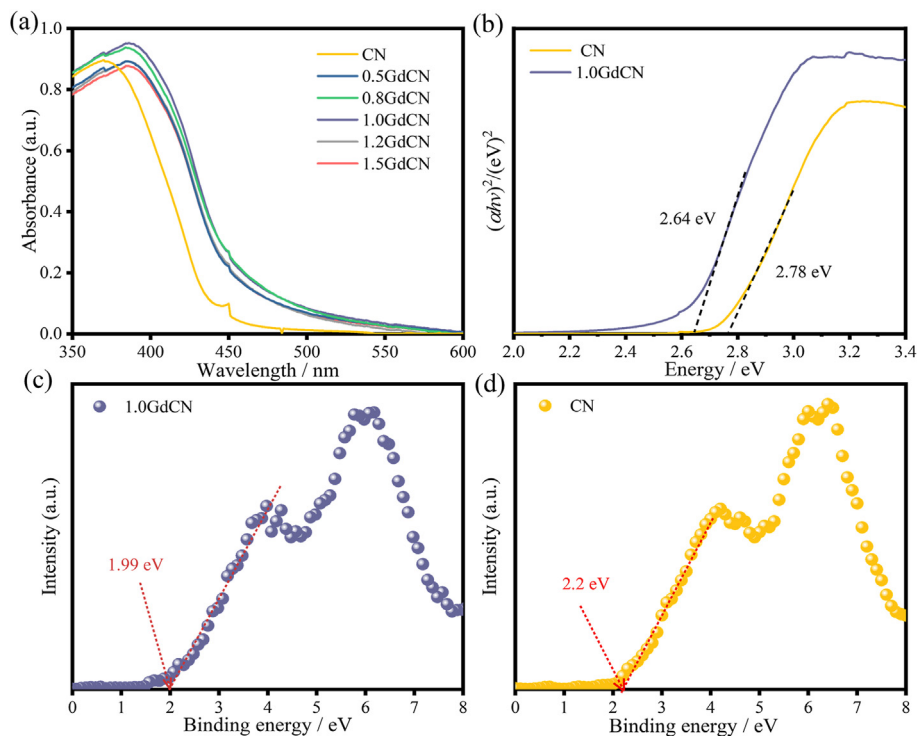


**Fig. 3.** (a) UV-vis DRS of CN and 1.0GdCN; (b) Corresponding plots of transformed Kubelka–Munk function versus photon energy of CN and 1.0GdCN; (c) VB-XPS spectra of 1.0GdCN and CN (d).

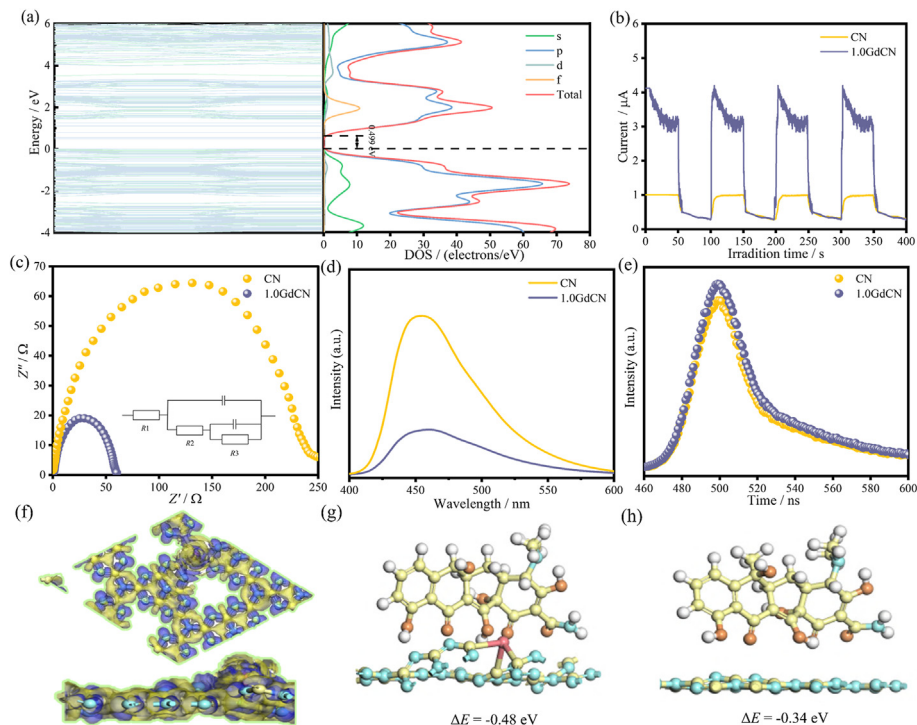


**Fig. 4.** (a) Projected state density and the total density of states and partial density of states of 1.0GdCN; (b) Transient photocurrent curves; (c) EIS; (d) Steady-state PL spectra; (e) TRPL decay spectra of the samples; (f) Differential charge density of 1.0GdCN. Blue: losing electrons, yellow: getting electrons; (h) Theoretical calculation of adsorption energy of tetracycline by 1.0GdCN (g) and CN.

resistance of 1.0GdCN is about 3.6 times that of pure CN, so the conductivity of 1.0GdCN photocatalyst is much higher than that of CN. In addition, the instantaneous photocurrent response curve reflects the ability of different photocatalysts to produce electron and hole pairs. As shown in Fig. 4(c), during the experimental operation, the time interval between the light source on and off is 50 s. When the light is turned on, both 1.0GdCN and CN show a clear photocurrent signal until it falls to the background value of the next light off. It is worth noting that 1.0GdCN has a stronger photocurrent intensity, which is much higher than that of CN. The results show that with the doping of Gd elements, the carrier separation ability of 1.0GdCN excited by light is improved, and the conductivity efficiency of the photocatalyst is enhanced, which is consistent with the above EIS description. It can also be speculated that more photogenerated charges in 1.0GdCN may participate in the photocatalytic reaction.

Secondly, the ability of charge generation, electron separation and transfer of the prepared photocatalyst can be explored by photoluminescence analysis. As shown in Fig. 4(d), it can be found that the strength signal value of 1.0GdCN is much smaller than that of CN. Therefore, the recombination rate of carriers produced by 1.0GdCN after light excitation is lower. It is worth noting that the main emission peaks of 1.0GdCN and CN are near 460 nm, which may be due to the result of N vacancy. The decay of the fluorescence lifetime of the photocatalyst is shown in Fig. 4(e). It is worth noting that the fluorescence lifetime of 1.0GdCN is not better than that of CN, but the electron availability of 1.0GdCN photocatalyst is stronger than that of CN. Combined with the above electrochemical impedance, photocurrent measurement and steady-state fluorescence, we can prove our preliminary conjecture that there may be more photogenerated charges in 1.0GdCN. At the same time, the experimental results show that 1.0GdCN with appropriate concentration can promote the effective separation of photogenerated

carrier, accelerate its migration to the surface of photocatalyst, enhance the electron work effect, and thus obtain good photocatalytic activity.

Lastly, the densities of states of 1.0GdCN and CN and the adsorption of tetracycline were obtained by theoretical calculation. Fig. 4(f) and Fig. S8 show the differential charge of 1.0GdCN and CN. The implantation of Gd element has significant effect on the charge density difference, and local electron localization occurs on the surface of 1.0GdCN photocatalyst. On the contrary, for CN, there is little impact. This is consistent with the results speculated by XPS description. In addition, the photocatalytic performance of GdCN system has been improved. The adsorption of tetracycline by 1.0GdCN and CN were shown in Fig. 4(f, g), respectively. Among them, the adsorption energy of CN to TC is  $-0.34$  eV, it is worth noting that the adsorption energy of 1.0GdCN is only  $-0.48$  eV. Therefore, the potential adsorption performance of 1.0GdCN is better. It is shown that with the doping of Gd, the local aggregation of electrons occurs on the surface of Gd which substitutes bridged nitrogen, resulting in electron localization, thus promoting electron transfer.

#### 3.4. Photocatalytic degradation of TC and its degradation pathway

In order to evaluate the photocatalytic effect of the prepared photocatalyst, we used TC as the degradation target. As shown in Fig. S9, TC can hardly be degraded without light, indicating that it has a certain degree of stability. As shown in Fig. 5(a), the degradation rate of CN in 18 min is only 29%, indicating that the degradation effect of CN on TC is very general. It is worth noting that the degradation rate of 1.0GdCN is up to 95%, which is much higher than that of pure CN, indicating that 1.0GdCN has the best degradation effect. In addition, other proportion of photocatalysts has different degrees of conversion. Among them, the degradation rate

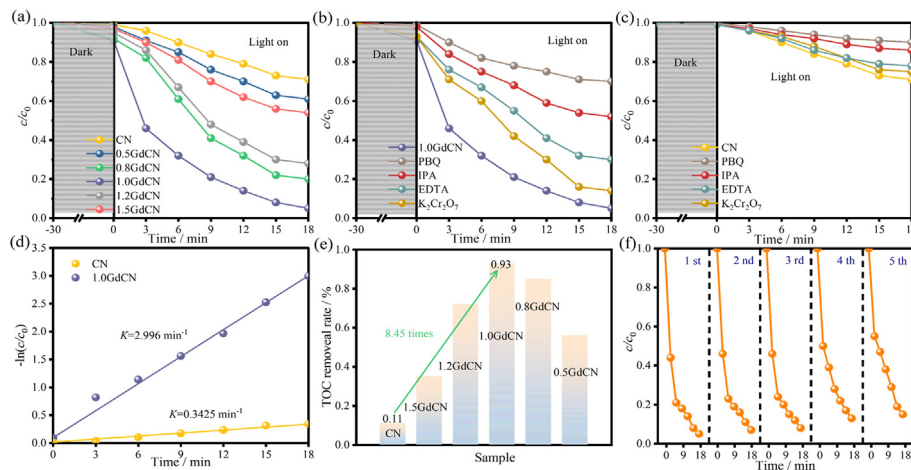


**Fig. 5.** Photocatalytic removal efficiency of TC over CN, 0.5GdCN, 0.8GdCN, 1.0GdCN, 1.2GdCN, and 1.5GdCN; photocatalytic capture experiments of 1.0GdCN (b) and CN (c); (d) Pseudo-first-order kinetic plots; (e) Total organic carbon test of samples; (f) Cyclic experiment of 1.0GdCN.

of 0.5GdCN and 0.8GdCN increased gradually, which may be due to the increase of the active center of the reaction with the increase of Gd content. On the contrary, the degradation rate of 1.2GdCN and 1.5GdCN decreased gradually, which may be due to the excessive content of Gd and the masking of the active center of the reaction. Interestingly, the conversion rate of 1.5GdCN is obviously higher than that of 0.5GdCN.

In order to explore the possible active substances in photocatalytic reaction, we carried out capture experiments. As shown in Fig. 5(b, c), 1 mL  $K_2Cr_2O_7$  (0.1 mg/L), 1 mL TEOA (0.1 mg/L), 1 mL PBQ (0.1 mg/L) and 1 mL IPA (0.1 mg/L) are used as quenchants for electron ( $e^-$ ), hole ( $h^+$ ), superoxide radical ( $O_2^-$ ) and hydroxyl radical ( $\bullet OH$ ). It is worth noting that with the addition of PBQ trapping agent, the photocatalytic effect of 1.0GdCN and CN on TC is the most significant, and the degradation rate in 18 min is only 30% and 10%, respectively. The second is IPA catcher, which makes the degradation rate become 48% and 14%. However, the other trapping agents had no obvious effect on the degradation rate of TC. To sum up, the main active substances for the degradation of TC by 1.0GdCN and CN are  $O_2^-$  and  $\bullet OH$ .

The kinetics of the photocatalytic TC degradation reaction were calculated according to Eq. (4):

$$K = \ln \frac{c_0}{c_t} / t \quad (4)$$

where  $K$  is the apparent rate constant (mol/min),  $c_0$  the initial pollutant concentration (mg/L) and  $c_t$  every time pollutant concentration (mg/L). As shown in Fig. 5(d), the apparent rate constant of 1.0GdCN ( $K = 2.996 \text{ min}^{-1}$ ) was the highest, which was about 8.25 times higher than that of CN ( $K = 0.3425 \text{ min}^{-1}$ ). The improvement of photocatalytic performance may be due to the introduction of N vacancy and Gd element and promoted the degradation of TC as the reaction center.

Finally, taking the removal efficiency of TOC as the evaluation index, the mineralization performance of photocatalyst for organic pollutants was investigated. As shown in Fig. 5(e), after 18 min is excited by visible light, the TOC removal efficiency of 1.0GdCN samples is 93%, which is 8.45 times higher than that of CN (0.11). It is proved that the catalyst has certain mineralization characteristics. In order to verify the stability of 1.0GdCN photocatalyst sample in TC oxidation, the stability of 1.0GdCN photocatalyst was evaluated by cycle test. As shown in Fig. 5(f), after 5 cycles for 4 h, the degradation rate of TC can still reach 85%. The experimental results

show that the sample has good reusability, and no obvious deactivation is observed. In addition, both 1.0GdCN and CN have good hydrophilicity, which is beneficial to the adsorption-desorption equilibrium of photocatalysts (Fig. S10). In order to verify its effectiveness, the photocatalytic degradation effects of different concentrations of TC and different grams of 1.0GdCN were also studied (Fig. S11). The TC concentrations of Fig. S11(a) were 5, 10 and 20 mg/L, respectively. The experimental results show that the TC solution of 5 mg/L can be degraded in 18 min, while the degradation rate of TC solution of 20 mg/L in 18 min is 68%. The reason may be that with the increase of TC concentration, the solution becomes more turbid, and the turbid liquid masks the position of the active center of the photocatalyst, resulting in the decrease of active species, thus weakening the photocatalytic performance. As shown in Fig. S11(b), the control experiments of different catalytic doses and 10 mg/L TC were carried out, and the results showed that the degradation rate of 0.2 g 1.0GdCN in 18 min reached 100%. The degradation rate of 0.05 g 1.0GdCN photocatalyst in 18 min is 80%. This may be because with the decrease of the amount of photocatalyst, the number of active sites will decrease, thus reducing the photocatalytic performance. In addition, the effectiveness of the 1.0GdCN cloth at pH values ranging from 4 to 10 was evaluated (Fig. S11(c)). Clearly, 89.9%, 94.8%, 95%, 92.4%, and 95.6% TC mitigation was achieved at pH values of 4, 5.5, 7.0, 8.5, and 10, respectively, using 1.0GdCN, signifying its attractive pH adaptability.

In order to understand the behavior of each atom in TC during photocatalysis, the density functional theory calculation of TC molecule was used to predict the bond breakage (Fig. 6). As shown in Fig. 6(b and c), the LUMO and HOMO of TC can explain the electron-deficient and rich-electron sites, respectively. Obviously, the  $-CH_3$  on the branch shows less electron deficiency, and the electrons tend to gather on the benzene ring of the TC molecule. In order to better determine the reactivity of each atom, their Fukui index was calculated (Table S5). The Fukui function is an effective method to predict the atomic reaction tendency, in which the  $f$  value is calculated according to the electron density difference between the normal state and the absence of an electron and the  $f^+$ -value refers to the electron density difference between the normal state and one more electron. In theory, higher  $f^0$ ,  $f^+$ , and  $f^-$  values of atoms refer to more vulnerable free radical attacks (through  $\bullet OH$ ), nucleophilic attacks (through  $O_2^-$ ), and electrophilic attacks (through  $^1O_2$  and  $\bullet OH$ ), respectively. Fig. 6(e-g) visualized the different reaction sites. Generally speaking, the left two



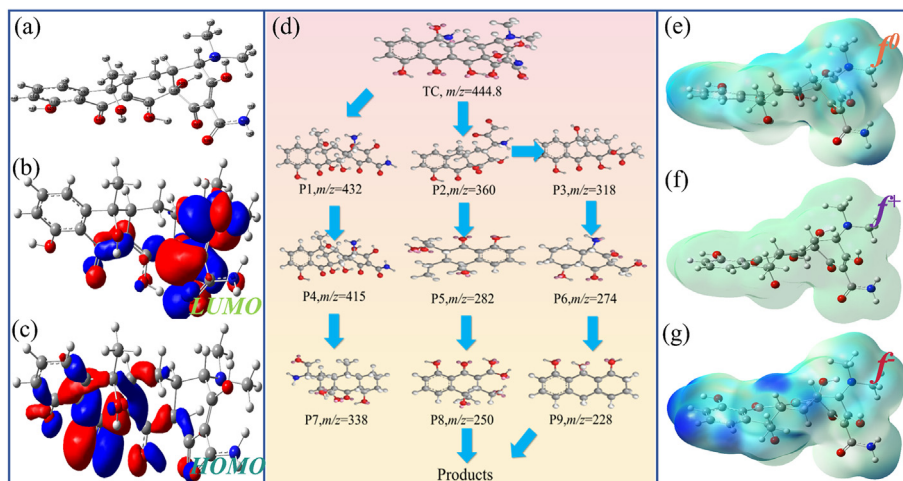


**Fig. 6.** (a) Atom numbering of TC; LUMO (b) and HOMO (c) of TC molecule; (d) Possible TC photodegradation pathway over 1.0GdCN;  $f^0$  (e),  $f^+$  (f), and  $f^-$  (g) index isosurface on TC molecule.

benzene rings in the TC structure are more active, whether for free radical reaction, electrophilic reaction or nucleophilic reaction. This result is consistent with the measurement of atomic reactivity by CDD value. No matter what the reaction type is, the benzene ring has relatively high reaction activity. On the other hand, the  $-\text{CH}_3$  on the side chain is more favorable for the reaction with  $^1\text{O}_2$  and  $\bullet\text{OH}$ . Interestingly, this electrophilic reaction in the side chain can correspond to the detection of active species: the higher contribution of  $\bullet\text{OH}$  may be due to its ability to destroy the side chain of TC.

The intermediates produced by the system during the degradation of TC were detected by LC-MS (Fig. 6(d)). The change of TC ( $m/z = 444.8$ ) abundance detected by LC-MS (Fig. S12) was consistent with that of TC measured by high performance liquid chromatography (Fig. S13): in the absence of light, 1.0GdCN had no effect on the degradation of TC in the dark reaction for 30 min, while 95% of TC could be effectively eliminated after photocatalytic degradation for 18 min. Table S6 summarizes the information about the main intermediates based on the mCompz detected by LC-MS. The elimination of TC in this system mainly produces 14 intermediates, which can be simply divided into three degradation pathways according to their main reaction types. First of all, the path I:P1 is due to the degradation of a  $-\text{CH}_3$  branch of TC, and then it may be due to  $\bullet\text{OH}$  attacking another  $-\text{CH}_3$  (free radical attack) to form P4. Finally, mainly due to the interaction between  $^1\text{O}_2$  and part of  $\bullet\text{OH}$ , the benzene ring breaks and forms P7. Path II and III underwent nucleophilic attack and electrophilic attack respectively, and finally mineralized P8 and P9 into  $\text{H}_2\text{O}$  and  $\text{CO}_2$ . To sum up, the abundance of P7 is stronger than that of P8 and P9, which is due to the back-and-forth transformation between  $\bullet\text{OH}$  and benzene ring with electron-rich state. As predicted by the Fukui index, the  $-\text{CH}_3$  in TC showed calm reactivity. In the degradation pathway I of TC, its decomposition mainly comes from  $-\text{CH}_3$ , accompanied by ring-breaking to form P7. Similarly, the intermediates in the II and III pathways come from the elimination reaction, but the hydrogen atoms on the side chain are still electrophilic attacked and directly broken before demethylation.

### 3.5. Reaction mechanism study

Firstly, in order to further explore the mechanism of TC degradation, we adopted the following strategies. As shown in Fig. 7(a–d), the peak  $\text{H}_2\text{O}_2$  signal intensity of 1.0GdCN increases

significantly with the prolonging time within 18 min, and the ability of CN to generate  $\text{H}_2\text{O}_2$  is much less than that of 1.0GdCN. It is worth noting that during the 15–18 min period, the production capacity of 1.0GdCN and CN photocatalysts entered a slow fatigue period, indicating that  $\text{H}_2\text{O}_2$  provided more power for photocatalytic degradation of TC during this period. At the same time, we measured the productivity of hydroxyl radical ( $\bullet\text{OH}$ ). As shown in Figs. S14 and 1.0GdCN reacted more strongly to  $\bullet\text{OH}$  within 18 min, much more than CN. It is worth noting that considering that the energy band structure of 1.0GdCN is  $E_{\text{CB}} = -1.99$  eV, which meets the requirements of transformation of  $\bullet\text{OH}/\text{OH}^-$  (1.99 eV), which is consistent with the ESR test results. It is worth noting that considering that the energy band structure of 1.0GdCN is  $E_{\text{CB}} = -1.99$  eV, which meets the requirements of  $\bullet\text{OH}/\text{OH}^-$  (1.99 eV) transformation, which is consistent with the ESR test results. Therefore, we can get the following equation:



Afterwards, the active species labeling under light is detected by electron spin resonance technique. As shown in Fig. 7(e, f) and Fig. S15, the peak intensity of 1.0GdCN is significantly enhanced, indicating the increased amount of  $\bullet\text{O}_2^-$  compared with CN. The generation trend of  $^1\text{O}_2$  in 1.0GdCN photocatalyst is consistent with that of superoxide anion radicals, and the yield is much higher than that of CN. Furthermore, no  $\bullet\text{O}_2^-$  and  $^1\text{O}_2$  signals were detected in the dark in the presence of 1.0GdCN and CN.

Finally, as we all know, the construction of activated oxygen sites is also one of the important factors affecting photocatalytic degradation. Fig. 7(g) shows the adsorption and desorption of oxygen by 1.0GdCN and CN at different temperatures. Interestingly, with the change of temperature, the oxygen adsorption and desorption ability of 1.0GdCN is similar to that of CN, but the oxygen peak area is wider and larger, indicating that 1.0GdCN has a better ability to activate and adsorb oxygen and transform into reactive oxygen species. It is worth noting that the maximum adsorption peak is at about 195 °C, which is due to the effect of nitrogen vacancy. Therefore, the nitrogen vacancy also has a certain effect on the adsorption of oxygen. Combined with Fig. 7(h, i), the oxygen adsorption energies of 1.0GdCN and CN photocatalysts are  $-0.6$  and  $-0.4$  eV respectively, which shows that the oxygen activation

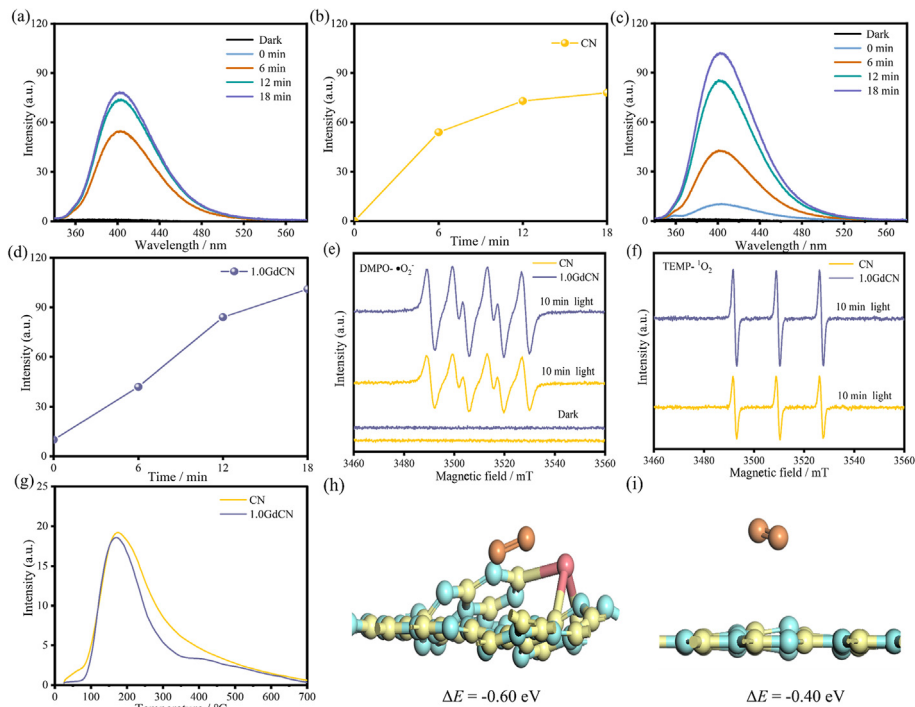
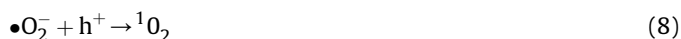
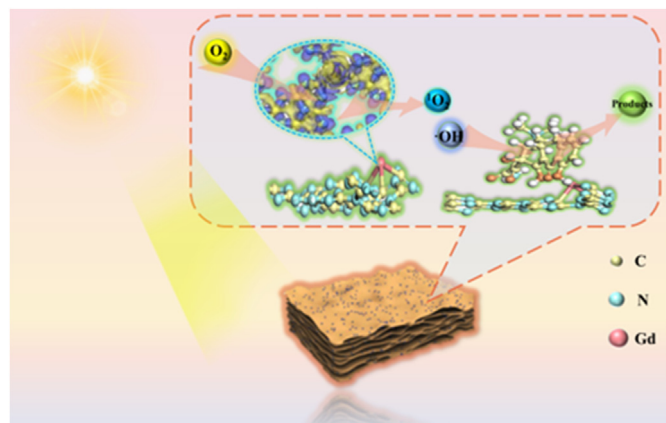


**Fig. 7.** H<sub>2</sub>O<sub>2</sub> production of CN (a, b) and 1.0GdCN (c, d); (e) DMPO-•O<sub>2</sub><sup>-</sup> adducts; (f) TEMP-<sup>1</sup>O<sub>2</sub> adducts; (g) TPD-O<sub>2</sub> of sample; Theoretical calculation of oxygen adsorption of 1.0GdCN (h) and CN (i).

ability is significantly enhanced and the oxygen activation site is successfully constructed. Therefore, combined with the above, it is shown that the Gd site is dissolved by oxygen in the degradation solution to produce •O<sub>2</sub><sup>-</sup>, which is further oxidized by holes to form <sup>1</sup>O<sub>2</sub>.<sup>52,53</sup>



To sum up, Scheme 1 reveals the electron transfer mechanism of photocatalytic degradation of TC pollutants. Under visible light irradiation, 1.0GdCN photocatalyst produced photogenerated



**Scheme 1.** The proposed photocatalytic remove mechanism of TC in 1.0GdCN.

electrons and holes, which were rapidly separated and localized on Gd elements. Oxygen in the air was dissolved in the degradation solution, then converted into superoxide free radicals, and then further oxidized to <sup>1</sup>O<sub>2</sub> by holes. Interestingly, during this period, the resulting H<sub>2</sub>O<sub>2</sub> is broken down into •OH. Finally, these active substances mineralize TC into water and carbon dioxide.

#### 4. Conclusions

Gd doped CN photocatalysts were prepared by simple thermal polymerization. Compared with CN, the photocatalytic degradation rate of TC by 1.0GdCN modified by Gd element is increased from 29% to 95%. The introduction of doped Gd not only broadens the optical response range of 1.0GdCN, but also effectively suppresses the recombination of photogenerated carriers. According to the theoretical calculations, nitrogen sites are occupied by Gd ions, which leads to the local electronation of Gd sites. In addition, photoelectrochemical characterizations show that the transfer of photogenerated charge has been improved. Therefore, the optimized photogenerated carrier dynamics and the expanded optical absorption range accelerate the formation of ROSs, thereby enhancing the photocatalytic performance for degrading TC by 1.0GdCN. Finally, the photocatalytic degradation pathway of TC was revealed by high performance liquid chromatography-mass spectrometry and density functional theory calculation. This study has laid a certain basic significance for element doping to improve photocatalytic wastewater treatment.

#### Declaration of competing interest

The authors declare that they have no known competing financial interests or personal relationships that could have appeared to influence the work reported in this paper.

## Acknowledgments

This work was also supported by Shaoguan Science and Technology Projects (220606154533827, 230616088031998, 200811094530440), and the Support Scheme of Guangzhou for Leading Talents in Innovation and Entrepreneurship Funding (2016015).

## Appendix A. Supplementary data

Supplementary data to this article can be found online at <https://doi.org/10.1016/j.jre.2024.02.008>.

## References

- Zhu Q, Hailili R, Xin Y, Zhou Y, Huang Y, Pang X, et al. Efficient full spectrum responsive photocatalytic NO conversion at Bi<sub>2</sub>Ti<sub>2</sub>O<sub>7</sub>: Co-effect of plasmonic Bi and oxygen vacancies. *Appl Catal B Environ.* 2022;319:121888.
- Zhu Q, Dar AA, Zhou Y, Zhang K, Qin J, Pan B, et al. Oxygen vacancies promoted piezoelectricity toward piezo-photocatalytic decomposition of tetracycline over SrBi<sub>4</sub>Ti<sub>4</sub>O<sub>15</sub>. *ACS ES&T Eng.* 2022;2:1365.
- Zhu Q, Zhang K, Li D, Li N, Xu J, Bahnemann DW, et al. Polarization-enhanced photocatalytic activity in non-centrosymmetric materials based photocatalysis: a review. *Chem Eng J (Amsterdam, Neth).* 2021;426:1311681.
- Wang S, Wang J. Single atom cobalt catalyst derived from co-pyrolysis of vitamin B12 and graphitic carbon nitride for PMS activation to degrade emerging pollutants. *Appl Catal B Environ.* 2023;321:122051.
- Tang R, Zeng H, Gong D, Deng Y, Xiong S, Li L, et al. Thin-walled vesicular triazole-CN-PDI with electronic n→π\* excitation and directional movement for enhanced atrazine photodegradation. *Chem Eng J (Amsterdam, Neth).* 2023;451:138445.
- Shang Y, Jiang N, Liu Z, Li C, Sun H, Guo H, et al. Pulsed discharge plasma assisted with Z-scheme graphene-TiO<sub>2</sub>-MnFe<sub>2</sub>O<sub>4</sub> for simultaneous removal of atrazine and Cr (VI): performance and mechanism. *Chem Eng J (Amsterdam, Neth).* 2023;452:139342.
- Luo J, Han H, Wang X, Qiu X, Liu B, Lai Y, et al. Single-atom Nb anchored on graphitic carbon nitride for boosting electron transfer towards improved photocatalytic performance. *Appl Catal B Environ.* 2023;328:122495.
- Feng C, Ouyang X, Deng Y, Wang J, Tang L. A novel g-C<sub>3</sub>N<sub>4</sub>/g-C<sub>3</sub>N<sub>4-x</sub> homojunction with efficient interfacial charge transfer for photocatalytic degradation of atrazine and tetracycline. *J Hazard Mater.* 2023;441:129845.
- Deng Y, Zhou Z, Zeng H, Tang R, Li L, Wang J, et al. Phosphorus and potassium codoped g-C<sub>3</sub>N<sub>4</sub> with multiple-locus synergies to degrade atrazine: insights into the depth analysis of the generation and role of singlet oxygen. *Appl Catal B Environ.* 2023;320:121942.
- Nazeri M, Sedaghat H, Rafiei R, Farzin MA, Mashkani SMH. Er<sub>2</sub>TiO<sub>5</sub>@Ag nanocomposites: enhanced photocatalysis and bacteria inactivation, and cytotoxicity. *J Rare Earths.* 2023;23:00295.
- Tang R, Gong D, Zhou Y, Deng Y, Feng C, Xiong S, et al. Unique g-C<sub>3</sub>N<sub>4</sub>/PDI-g-C<sub>3</sub>N<sub>4</sub> homojunction with synergistic piezo-photocatalytic effect for aquatic contaminant control and H<sub>2</sub>O<sub>2</sub> generation under visible light. *Appl Catal B Environ.* 2022;303:120929.
- Ding P, Ji H, Li P, Liu Q, Wu Y, Guo M, et al. Visible-light degradation of antibiotics catalyzed by titania/zirconia/graphitic carbon nitride ternary nanocomposites: a combined experimental and theoretical study. *Appl Catal B Environ.* 2022;300:120633.
- Luo J, Han H, Wang X, Lai Y, Liu B, Zhong R, et al. Constructing oxygen absorption and activation sites in Ce-doped g-C<sub>3</sub>N<sub>4</sub> photocatalyst for effective removal of amoxicillin: performance, mechanism and degradation pathways. *Appl Surf Sci.* 2023;611:155808.
- Haron A, Anwar K, Ahmed AS. Visible light-driven photo remediation of hazardous cationic dye via Ce-doped WO<sub>3</sub> nanostructures. *J Rare Earths.* 2023;23:00319.
- Han H, Wang X, Qiao Y, Lai Y, Liu B, Zhang Y, et al. Construction of S-scheme heterojunction for enhanced photocatalytic conversion of NO over dual-defect CeO<sub>2-x</sub>/g-C<sub>3</sub>N<sub>4-x</sub>. *J Alloys Compd.* 2023;933:167819.
- Luo J, Han H, Wu J, Wang X, Feng J, Toan S, et al. Excellent photocatalytic activity of MoO<sub>3</sub>-adorned g-C<sub>3</sub>N<sub>4</sub> systems: construction of S-scheme heterojunction. *Appl Surf Sci.* 2022;604:154512.
- Zhao C, Meng L, Chu H, Wang J-F, Wang T, Ma Y, et al. Ultrafast degradation of emerging organic pollutants via activation of peroxymonosulfate over Fe<sub>3</sub>C/Fe@N-C-x: singlet oxygen evolution and electron-transfer mechanisms. *Appl Catal B Environ.* 2023;321:122034.
- Zhang W, Zhang S, Meng C, Zhang Z. Nanoconfined catalytic membranes assembled by cobalt-functionalized graphitic carbon nitride nanosheets for rapid degradation of pollutants. *Appl Catal B Environ.* 2023;322:122098.
- Zhang M, Lin X, Yi Z, Xu X, Yang J, Zhu M. Enhanced reactive oxidation species generation by ligand-to-metal-charge transfer between oxygen vacancy-rich ZnO mesocrystal with ciprofloxacin pollutants. *Appl Catal B Environ.* 2023;321:122033.
- Wang M, Tan G, Zhang B, Wang Y, Bi Y, Yang Q, et al. Synergistic integration of energy storage catalysis: a multifunctional catalytic material for round-the-clock environmental cleaning. *Appl Catal B Environ.* 2023;321:122052.
- Hu Y, Nie M, Hong P, He J, Li Y, Zhang K, et al. Defect-engineered WO<sub>3-x</sub>@MoS<sub>2</sub> hollow tube exhibiting enhanced Fenton-like and photocatalytic activities via electric field rearrangement and band alignment. *Appl Catal B Environ.* 2023;320:122013.
- Yu Y, Xu W, Fang J, Chen D, Pan T, Feng W, et al. Soft-template assisted construction of superstructure TiO<sub>2</sub>/SiO<sub>2</sub>/g-C<sub>3</sub>N<sub>4</sub> hybrid as efficient visible-light photocatalysts to degrade berberine in seawater via an adsorption-photocatalysis synergy and mechanism insight. *Appl Catal B Environ.* 2020;268:118751.
- Zhang Q, Jiang L, Wang J, Zhu Y, Pu Y, Dai W. Photocatalytic degradation of tetracycline antibiotics using three-dimensional network structure perylene diimide supramolecular organic photocatalyst under visible-light irradiation. *Appl Catal B Environ.* 2020;277:119122.
- Huang S, Zhang Q, Liu P, Ma S, Xie B, Yang K, et al. Novel up-conversion carbon quantum dots/α-FeOOH nanohybrids eliminate tetracycline and its related drug resistance in visible-light responsive Fenton system. *Appl Catal B Environ.* 2020;263:118336.
- Du P, Hu K, Lyu J, Li H, Lin X, Xie G, et al. Anchoring Mo single atoms/clusters and N on edge-rich nanoporous holey graphene as bifunctional air electrode in Zn-air batteries. *Appl Catal B Environ.* 2020;276:119172.
- Mirzaei A, Chen Z, Haghghat F, Yerushalmi L. Magnetic fluorinated mesoporous g-C<sub>3</sub>N<sub>4</sub> for photocatalytic degradation of amoxicillin: transformation mechanism and toxicity assessment. *Appl Catal B Environ.* 2019;242:337.
- Adhikari S, Selvaraj S, Kim D-H. Construction of heterojunction photoelectrode via atomic layer deposition of Fe<sub>2</sub>O<sub>3</sub> on Bi<sub>2</sub>WO<sub>6</sub> for highly efficient photoelectrochemical sensing and degradation of tetracycline. *Appl Catal B Environ.* 2019;244:11.
- Wang W, Fang J, Shao S, Lai M, Lu C. Compact and uniform TiO<sub>2</sub>/g-C<sub>3</sub>N<sub>4</sub> core-shell quantum heterojunction for photocatalytic degradation of tetracycline antibiotics. *Appl Catal B Environ.* 2017;217:57.
- Xu L, Li L, Hu Z, Yu JC. Boosting alkaline photocatalytic H<sub>2</sub>O<sub>2</sub> generation by incorporating pyrophosphate on g-C<sub>3</sub>N<sub>4</sub> for effective proton shuttle and oxygen activation. *Appl Catal B Environ.* 2023;328:122490.
- Shen R, Liu Y, Zhang H, Liu S, Wei H, Yuan H, et al. Coupling oxygen vacancy and hetero-phase junction for boosting catalytic activity of Pd toward hydrogen generation. *Appl Catal B Environ.* 2023;328:122484.
- Miao Y, Li Z, Song Y, Fan K, Guo J, Li R, et al. Surface active oxygen engineering of photoanodes to boost photoelectrochemical water and alcohol oxidation coupled with hydrogen production. *Appl Catal B Environ.* 2023;323:122147.
- Li Y-W, Li S-Z, Liu L-Y, Zhang Z-F, Ma W-L. Bi modified oxidized tubular carbon nitride with high-yield singlet oxygen for propylparaben degradation: implication for a novel oxygen activation mechanism. *Appl Catal B Environ.* 2023;321:122025.
- Gao K, Hou L-a, An X, Huang D, Yang Y. BiOBr/MXene/g-C<sub>3</sub>N<sub>4</sub> Z-scheme heterostructure photocatalysts mediated by oxygen vacancies and MXene quantum dots for tetracycline degradation: process, mechanism and toxicity analysis. *Appl Catal B Environ.* 2023;323:122150.
- Zhang C, Qin D, Zhou Y, Qin F, Wang H, Wang W, et al. Dual optimization approach to Mo single atom dispersed g-C<sub>3</sub>N<sub>4</sub> photocatalyst: morphology and defect evolution. *Appl Catal B Environ.* 2022;303:120904.
- Wei X, Feng H, Li L, Gong J, Jiang K, Xue S, et al. Synthesis of tetragonal prismatic γ-In<sub>2</sub>Se<sub>3</sub> nanostructures with predominantly {110} facets and photocatalytic degradation of tetracycline. *Appl Catal B Environ.* 2020;260:118218.
- Li H, Sun S, Ji H, Liu W, Shen Z. Enhanced activation of molecular oxygen and degradation of tetracycline over Cu-S<sub>4</sub> atomic clusters. *Appl Catal B Environ.* 2020;272:118966.
- Xu Y, Pan Y, Yahan W, Fang Y, Anpo M, Yoshida H, et al. Photoanodic H<sub>2</sub>O<sub>2</sub> synthesis and in-situ tetracycline degradation using transition-metal phosphide co-catalysts. *Appl Catal B Environ.* 2023;331:122701.
- Tang R, Zeng H, Deng Y, Xiong S, Li L, Zhou Z, et al. Dual modulation on peroxymonosulfate activation site and photocarrier separation in carbon nitride for efficient photocatalytic organics degradation: efficacy and mechanism evaluation. *Appl Catal B Environ.* 2023;336:122918.
- Zhang Z, Liang J, Zhang W, Zhou M, Zhu X, Liu Z, et al. Modified-pollen confined hybrid system: a promising union for visible-light-driven photocatalytic antibiotic degradation. *Appl Catal B Environ.* 2023;330:122621.
- Zhang W, Zhang S, Meng C, Zhang Z. Nanoconfined catalytic membranes assembled by cobalt-functionalized graphitic carbon nitride nanosheets for rapid degradation of pollutants. *Appl Catal B Environ.* 2023;322:122098.
- Yue J, Yang H, Liu C, Zhang Q, Ao Y. Constructing photocatalysis-self-Fenton system over a defective twin C<sub>3</sub>N<sub>4</sub>: in-situ producing H<sub>2</sub>O<sub>2</sub> and mineralizing organic pollutants. *Appl Catal B Environ.* 2023;331:122716.
- Yang Y, Yu H, Wu M, Zhao T, Guan Y, Yang D, et al. Dual H<sub>2</sub>O<sub>2</sub> production paths over chemically etched MoS<sub>2</sub>/FeS<sub>2</sub> heterojunction: maximizing self-sufficient heterogeneous Fenton reaction rate under the neutral condition. *Appl Catal B Environ.* 2023;325:122307.
- Su L, Wang P, Li M, Zhao Z, Li Y, Zhan S. Synergistic enhancement of photocatalytic molecular oxygen activation by nitrogen defect and interfacial photoelectron transfer over Z-scheme α-Fe<sub>2</sub>O<sub>3</sub>/g-C<sub>3</sub>N<sub>4</sub> heterojunction. *Appl Catal B Environ.* 2023;335:122890.
- Ranjbari A, Demeestere K, Kim K-H, Heynderickx PM. Oxygen vacancy modification of commercial ZnO by hydrogen reduction for the removal of

- thiabenzazole: characterization and kinetic study. *Appl Catal B Environ.* 2023;324:122265.
45. Nguyen AQK, Ahn Y-Y, Shin G, Cho Y, Lim J, Kim K, et al. Degradation of organic compounds through both radical and nonradical activation of peroxy-monosulfate using CoWO<sub>4</sub> catalysts. *Appl Catal B Environ.* 2023;324:122266.
  46. Miao W, Yao D, Chu C, Liu Y, Huang Q, Mao S, et al. Highly-efficient photocatalytic H<sub>2</sub>O<sub>2</sub> evolution using hydrothermal carbons with donor-acceptor furan couples. *Appl Catal B Environ.* 2023;332:122770.
  47. Martínez-Huitle CA, Rodrigo MA, Sirés I, Scialdone O. A critical review on latest innovations and future challenges of electrochemical technology for the abatement of organics in water. *Appl Catal B Environ.* 2023;328:122430.
  48. Mao X, Wang M, Li J, Zhang M, Dong C, Lei H, et al. High atom utility of robust Ca-Co bimetallic catalyst for efficient Fenton-like catalysis in advanced oxidation processes. *Appl Catal B Environ.* 2023;331:122698.
  49. Li X, Hu J, Deng Y, Li T, Liu Z-Q, Wang Z. High stable photo-Fenton-like catalyst of FeP/Fe single atom-graphene oxide for long-term antibiotic tetracycline removal. *Appl Catal B Environ.* 2023;324:122243.
  50. Luo J, Li W, Wang X, Liu B, Zhang Y, Jiang M, et al. Ytterbium induced surface polarization of graphitic carbon nitride with N vacancies towards enhanced photocatalytic decomposition of tetracycline. *Appl Surf Sci.* 2024;644:158743.
  51. Moradi M, Hasanvandian F, Isari AA, Hayati F, Kakavandi B, Setayesh SR. CuO and ZnO co-anchored on g-C<sub>3</sub>N<sub>4</sub> nanosheets as an affordable double Z-scheme nanocomposite for photocatalytic decontamination of amoxicillin. *Appl Catal B Environ.* 2021;285:119838.
  52. Xu X, Wang J, Chen T, Yang N, Wang S, Ding X, et al. Deep insight into ROS mediated direct and hydroxylated dichlorination process for efficient photocatalytic sodium pentachlorophenate mineralization. *Appl Catal B Environ.* 2021;296:120352.
  53. Wang H, Jin S, Zhang X, Xie Y. Excitonic effects in polymeric photocatalysts. *Angew Chem, Int Ed.* 2020;59:22828.

## **Linker Gd as charge channel and singlet oxygen activation site in graphitic carbon nitride for enhancing photocatalytic decomposition of tetracycline**

### **Text S1. Catalysts characterization**

The morphology of the samples was acquired on a Zeiss Sigma 300 scanning electron microscope (SEM). Transmission electron microscopy (TEM) and energy disperse X-ray spectroscopy (EDS) were performed on FEI Tecnai F20 to characterize the microstructure and elemental distribution of the samples. Brunauer-Emmett-Teller (BET) and Barrett-Joyner-Halenda (BJH) methods were performed by a Micromeritics ASAP 2020 HD88 instrument. X-ray diffractometry (XRD) was performed by a Panalytical Empyrean powder diffractometer with Cu K $\alpha$  radiation, and the scanning range was between 10° to 80°. The Fourier transform infrared (FT-IR) spectra were obtained by the Thermo Scientific Nicolet iS5 spectrophotometer with the KBr pellet method. Electron paramagnetic resonance (EPR) was measured by the EPR spectrometer (JEOL JES-FA200). The contents of C and N elements were quantified by elemental analysis (EA, Vario MACRO cube analyzer). X-ray photoelectron spectroscopy (XPS) was performed using the Thermo Scientific K-Alpha spectrometer with an Al K $\alpha$  line source. UV-visible diffuse reflectance spectra (UV-vis DRS) were obtained by a Varian Cary 300 instrument. Photoluminescence (PL) emission spectra and time-resolved photoluminescence (TRPL) decay spectra were monitored by the Fluoromax-4 spectrophotometer and FLS1000 fluorescence lifetime spectrophotometer, respectively. Electron spin resonance (ESR) of reactive species was measured on a Bruker A300 spectrometer. The photoelectrochemical characterization was conducted by a CHI 660D workstation.

### **Text S2. Photoelectrochemical experiment**

The photoelectrochemical properties were carried out on a CHI 660E electrochemical workstation using a typical three-electrode system in an aqueous KCl electrolyte (0.5M). The photocatalysts were deposited on FTO glass (SnO<sub>2</sub> Transparent Conducting glass doped with fluorine) and used as working electrodes. The working electrode, counter electrode and reference electrode were the prepared sample, a platinum wire and the saturated calomel electrode (SCE). A 300W xenon lamp with a 420 nm cut-off filter was used as a light source. For preparing the working electrode, 10 mg of photocatalysts and 10  $\mu$ L of Nafion solution (5 wt%) were put mortar to get a homogeneous colloid. Then, the slurry was deposited onto the cleaned FTO glass (2.0 cm  $\times$  2.5 cm) and dried in air. The electrochemical impedance spectra (EIS) were performed between a frequency range from 10 MHz to 100 kHz by applying a 5-mV amplitude.

### Text S3. Active species trapping experiments

To detect the active species for the photocatalytic degradation of TC, different trapping reagents were employed by adding potassium dichromate ( $K_2Cr_2O_7$ , an electron scavenger), diethanolamine (TEOA, a hole scavenger), 1,4-benzoquinone (PBQ, a superoxide radical scavenger), and isopropyl alcohol (IPA, a hydroxyl radical scavenger) in the reaction solutions.

The  $H_2O_2$  was tested using the fluorescence method: 0.1 g of sample powder was added to a 200 mL beaker containing 100 mL of deionized water to form a sample suspension. Then, this suspension was irradiated by visible light with continuous stirring. The beaker was kept at a magnetic stirring apparatus during the irradiation. During irradiation, 3 mL of the suspension was taken from the beaker every 10 min. This suspension was centrifuged, and the sample partials were removed. Subsequently, 50  $\mu$ L of fluorescent reagent (its preparation is detailed in the Supporting Information) was added to react with the as-generated  $H_2O_2$ . After 10 min, 1 mL NaOH solution was added to end the reaction. Finally, the  $H_2O_2$  concentration was measured by a fluorescence spectrophotometer (emitted at 409 nm and excited at 315 nm).

As for the test of the  $\bullet OH$ , 0.1 g of the sample was dispersed into 100 mL of terephthalic acid solution (1.25 mol/L) and stirred in the dark for 30 min. Then, after turning on the visible light, 3 mL of the suspension was taken from the reacting beaker every 10 min. This suspension stood for 10 min, and then the sampled partials were removed for the fluorescence test (emitted at 426 nm and excited at 312 nm).

### Text S4. DFT detailed description

The Gd element doped  $g-C_3N_4$  were investigated by first-principles density-functional theory calculations using the DMol<sub>3</sub> module in Materials Studio. The adsorption energy of TC over CN and 1-Gd/CN are calculated. The electron exchange–functional is calculated using Perdew–Burke–Ernzerhof (PBE) described by the generalized gradient approximation (GGA). An all-electron double numerical atomic orbital augmented by Double Numerical plus d-functions (DND) was employed as basis set, and DFT semicore pseudopotentials (DSPPs) are used for interactions between the ion core and valence electrons. The convergence criteria for the total energy, maximum force, and maximum displacement were set to  $10^{-5}$  Hartree, 0.002 Hartree·Å<sup>-1</sup>, and 0.005 Å, respectively. The electronic self-consistent field (SCF) tolerance was set to  $10^{-6}$  Hartree. DFT calculations are carried out to investigate the required energy for several possible doped positions based on Eq. (S1):

where  $E_{total}$  is the energy of the possible structure calculated by DFT,  $E_{g-C_3N_4}$  refers to the energy of  $g-C_3N_4$  (-2245 eV), and  $E_{Nb}$  denotes the energy of Gd (-2245 eV). Accordingly, the interaction energy is defined as follows:

where  $E_{abs}$  is adsorption energy of TC on  $g-C_3N_4$  surface;  $E_{total}$  is the energy of TC and  $g-C_3N_4$ ;  $E_{g-C_3N_4}$  is the energy of  $g-C_3N_4$  and  $E_{TC}$  is the energy of TC, respectively. Additionally, the theoretical calculations were performed via the Gaussian 16 suite of programs. The structure of the studied compound (denoted by M) is fully optimized at the B3LYP-D3/def2-SVP level of theory. The vibrational frequencies of the optimized structures were carried out at the same level. The structures were characterized as a local energy minimum on the potential energy surface

$$E = E_{total} - E_{g-C_3N_4} - E_{Gd} \quad (S1) \quad \text{by}$$

$$E_{abs} = E_{total} - E_{g-C_3N_4} - E_{TC} \quad (S2)$$

verifying that all the vibrational frequencies were real. The molecular orbital levels including the highest occupied molecular orbital (HOMO) and the lowest unoccupied molecular orbital (LUMO), and the Fukui index of M were calculated at the B3LYP-D3/def-TZVP level and analyzed by using the Multiwfn software. The Visual Molecular Dynamics (VMD) program is used to plot the color-filled iso-surface graphs to visualize the molecular orbitals and Fukui functions. As a commonly used calculation tool to determine the active site, the Fukui function ( $f(r)$ ) is as follows:

$$f(r) = \left( \frac{\partial^2 E}{\partial N \cdot \partial v(r)} \right) = \left[ \frac{\partial \mu}{\partial v(r)} \right]_N = \left[ \frac{\partial \rho(r)}{\partial N} \right]_{V(r)} \quad (\text{S3})$$

where N refers to the number of electrons,  $\rho(r)$  represents the electron density at point r in space, and the constant term v in the partial derivative represents the external potential. According to three different scenarios (nucleophilic attack, electrophilic attack, and radical attack), the condensed Fukui function can be calculated by the following formula:

$$\text{Nucleophilic attack: } f_k^+ = q_N^k - q_{N+1}^k \quad (\text{S4})$$

$$\text{Electrophilic attack: } f_k^- = q_{N-1}^k - q_N^k \quad (\text{S5})$$

$$\text{Radical attack: } f_k^0 = (q_{N-1}^k - q_{N+1}^k) / 2 \quad (\text{S6})$$

where  $q^k$  represents the charge population of atom k. In general, the values of the concentrated Fukui function at the active sites are larger than those at other sites. Besides, the generalized gradient approximation (GGA) method with Perdew-Burke-Ernzerhof (PBE) function is employed to describe the interactions between core and electrons. The force and energy convergence criterion are set to  $0.002 \text{ Ha } \text{\AA}^{-1}$  and  $10^{-5} \text{ Ha}$ , respectively. When the optimization is completed, the HOMO and LUMO calculations were performed.

### Text S5. Detailed description of Kubelka-Munk equation

In order to further determine the photochemical absorption band of the material, the Kubelka-Munk equation was used to calculate the band gap of the photocatalyst material at the reflecting edge.

$$(\alpha h\nu)^{1/2} = A(h\nu - E_g) \quad (\text{S6})$$

Where  $\alpha$  is the absorption index, h is the Planck constant,  $\nu$  is the frequency, A is the constant,  $E_g$  is the bandgap width for semiconductors. In addition, the index n is directly related to the type of semiconductors. Direct Bandgap Semiconductors:  $n = \frac{1}{2}$ . Furthermore, it indicates meaning that Kubelka-Munk equation is a mathematical model that reflects the characteristics of absorption, scattering and transmission of matter. The equation describes the attenuation and scattering of light in a homogeneous medium.

Table S1. Surface area and pore size are summarized

Sample	Specific surface area (m <sup>2</sup> /g)	Pore size (nm)	Pore volume (cm <sup>3</sup> /g)
CN	8.6	19.7	0.085
1.0GdCN	13.3	25.2	0.065

Table S2. The area in XPS N 1 s spectrum of CN and 1.0GdCN peaks.

Sample	Bridge N	Triazine units N	Amino functional groups
CN	109261.43	40530.2	14579.64
1.0GdCN	97918.73	39909.62	11810.73



Table S3. Summary table of binding energy at each position after gadolinium doped carbon nitride

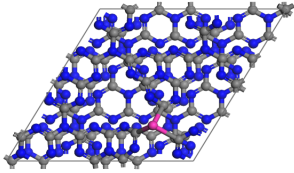
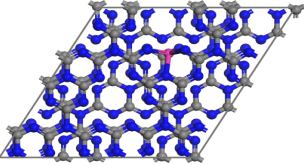
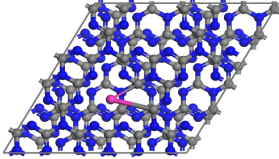
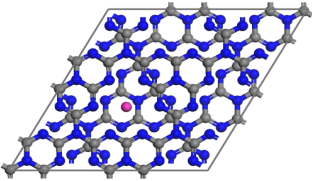
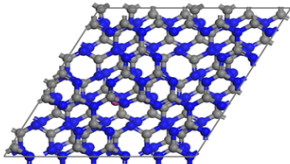
1.0GdCN	E (eV)
	-2901
	-3136
	-3415
	-3295
	-3136

Table S4. Electrochemical fitting comparison of CN and 1-Gd/CN.

Sample	Resistance (ohm)	Resistance (ohm)	Resistance (ohm)
CN	1.801	0.569	38.61
1.0GdCN	6.52	2.1048	139.327

Table S5. Condensed Fukui index distribution on 1.0GdCN.

Atom	q(N)	q(N+1)	q(N-1)	f-	f+	f0	CDD
1(C)	0.1494	0.0717	0.1601	0.0107	0.0777	0.0442	0.067
2(C)	-0.0442	-0.0822	-0.0394	0.0048	0.038	0.0214	0.0332
3(C)	0.1071	0.026	0.1198	0.0127	0.0811	0.0469	0.0684
4(C)	0.0276	0.0202	0.0301	0.0025	0.0075	0.005	0.005
5(C)	-0.0246	-0.0275	-0.023	0.0016	0.003	0.0023	0.0014
6(C)	-0.055	-0.0567	-0.0511	0.0039	0.0017	0.0028	-0.0022
7(C)	-0.0244	-0.0274	-0.0149	0.0095	0.003	0.0062	-0.0065
8(C)	0.0922	0.0909	0.0973	0.0051	0.0014	0.0032	-0.0038
9(C)	-0.0002	-0.0083	0.0111	0.0113	0.0081	0.0097	-0.0032
10(C)	-0.0567	-0.0701	-0.02	0.0367	0.0135	0.0251	-0.0232
11(C)	-0.0311	-0.0632	0.0076	0.0388	0.032	0.0354	-0.0067
12(C)	-0.0697	-0.0899	-0.04	0.0296	0.0203	0.025	-0.0094
13(C)	0.0949	0.0807	0.1201	0.0252	0.0142	0.0197	-0.011
14(C)	-0.0359	-0.0385	-0.0196	0.0163	0.0026	0.0094	-0.0137
15(C)	0.1227	0.0894	0.1548	0.0321	0.0332	0.0327	0.0011
16(C)	-0.0608	-0.0804	-0.0023	0.0585	0.0196	0.0391	-0.0389
17(C)	0.1044	0.0944	0.1459	0.0415	0.01	0.0257	-0.0314
18(C)	0.0696	0.0599	0.0785	0.0089	0.0097	0.0093	0.0008
19(C)	0.1704	0.1602	0.1779	0.0074	0.0103	0.0088	0.0028
20(O)	-0.2902	-0.3212	-0.2651	0.0251	0.0309	0.028	0.0058
21(N)	-0.1519	-0.172	-0.1322	0.0197	0.0201	0.0199	0.0004

---

22(O)	-0.2513	-0.3025	-0.1344	0.1169	0.0512	0.0841	-0.0657
23(O)	-0.2092	-0.305	-0.1687	0.0405	0.0958	0.0682	0.0553
24(C)	-0.084	-0.0884	-0.0765	0.0074	0.0044	0.0059	-0.003
25(O)	-0.2386	-0.2656	-0.2203	0.0183	0.0269	0.0226	0.0086
26(O)	-0.1522	-0.1717	-0.1001	0.052	0.0195	0.0358	-0.0325
27(O)	-0.1676	-0.1784	-0.1367	0.0309	0.0109	0.0209	-0.02
28(O)	-0.2304	-0.2384	-0.2091	0.0214	0.0079	0.0146	-0.0134
29(O)	-0.1507	-0.2009	-0.1321	0.0185	0.0502	0.0344	0.0317
30(N)	-0.0652	-0.0668	-0.0656	-0.0003	0.0016	0.0006	0.0019
31(C)	-0.0359	-0.0408	-0.0318	0.0041	0.005	0.0045	0.0009
32(C)	-0.0285	-0.0374	-0.0251	0.0034	0.0089	0.0062	0.0055
33(H)	0.0324	0.0163	0.0394	0.007	0.0161	0.0116	0.0091
34(H)	0.0205	0.0085	0.041	0.0206	0.012	0.0163	-0.0086
35(H)	0.021	0.0031	0.0305	0.0095	0.0179	0.0137	0.0085
36(H)	0.0212	0.0206	0.0264	0.0052	0.0007	0.0029	-0.0045
37(H)	0.024	0.0119	0.0384	0.0145	0.012	0.0133	-0.0024
38(H)	0.0347	0.0241	0.0547	0.02	0.0106	0.0153	-0.0094
39(H)	0.0417	0.0229	0.0664	0.0246	0.0188	0.0217	-0.0058
40(H)	0.0348	0.0188	0.0575	0.0227	0.016	0.0193	-0.0066
41(H)	0.109	0.0998	0.118	0.009	0.0092	0.0091	0.0002
42(H)	0.132	0.1091	0.1464	0.0144	0.0229	0.0187	0.0085
43(H)	0.0279	0.0208	0.0373	0.0094	0.0072	0.0083	-0.0022
44(H)	0.0345	0.0238	0.047	0.0125	0.0107	0.0116	-0.0018
45(H)	0.0298	0.0274	0.0404	0.0106	0.0024	0.0065	-0.0081
46(H)	0.1126	0.1033	0.1235	0.0109	0.0093	0.0101	-0.0017
47(H)	0.147	0.1375	0.1668	0.0198	0.0095	0.0147	-0.0104
48(H)	0.1763	0.1636	0.1987	0.0225	0.0127	0.0176	-0.0098
49(H)	0.1434	0.1428	0.1463	0.0029	0.0006	0.0018	-0.0023
50(H)	0.1795	0.1539	0.1902	0.0107	0.0255	0.0181	0.0149
51(H)	0.0332	0.0324	0.0347	0.0016	0.0008	0.0012	-0.0008

---

52(H)	0.0434	0.0266	0.0532	0.0098	0.0167	0.0133	0.0069
53(H)	0.0161	0.0041	0.0251	0.0089	0.0121	0.0105	0.0032
54(H)	0.0415	0.0356	0.0408	-0.0007	0.0059	0.0026	0.0066
55(H)	0.0427	0.0273	0.0521	0.0094	0.0154	0.0124	0.006
56(H)	0.0208	0.0061	0.03	0.0092	0.0147	0.0119	0.0054

Table S6. The possible intermediate products of photocatalytic TC degradation by 1.0GdCN sample under visible light irradiation.

Compounds	m/z	Proposed formula	Proposed structure
TC	444.8	$C_{22}H_{24}N_2O_8$	
TC 2	432	$C_{20}H_{20}N_2O_9$	
TC 3	415	$C_{18}H_{19}NO_7$	
TC 4	360	$C_{20}H_{20}N_2O_8$	
TC 5	338	$C_{19}H_{18}O_7$	
TC 6	318	$C_{17}H_{18}O_6$	
TC 7	282	$C_{20}H_{18}N_2O_7$	
TC 8	274	$C_{20}H_{17}NO_7$	
TC 9	250	$C_{18}H_{19}NO_6$	

TC 14

228

$C_9H_{12}O_3$

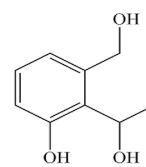


Table S7. Comparison of TC photocatalytic degradation activity with other g-C<sub>3</sub>N<sub>4</sub> based photocatalysts.

Photocatalyst	Dosage (g L <sup>-1</sup> )	Light source	Adsorption and photocatalytic time	Removal percentage
C <sub>3</sub> N <sub>4</sub> /B-C-dots	0.5	300 W Xenon lamp ( $\lambda > 420$ nm)	50 min + 180 min	98.73%
MoO <sub>3</sub> /Ag/ C <sub>3</sub> N <sub>4</sub>	1	150 W Xenon lamp ( $\lambda > 400$ nm)	120 min + 100 min	89%
Mo <sub>2</sub> C/CN	1	300 W Xenon lamp ( $\lambda > 420$ nm)	60 min + 60 min	91.6%
h-BN/g-C <sub>3</sub> N <sub>4</sub>	1	300 W Xenon lamp ( $\lambda > 420$ nm)	60 min + 60 min	79.7%
Ag/PCN	1.67	300 W Xenon lamp ( $\lambda > 420$ nm)	60 min + 120 min	83%
C-WO <sub>3</sub> -g-C <sub>3</sub> N <sub>4</sub>	1	300 W Xenon lamp ( $\lambda > 420$ nm)	30 min + 60 min	90.54%
0D MoO <sub>3</sub> /2D g-C <sub>3</sub> N <sub>4</sub>	0.5	300 W Xenon lamp ( $\lambda > 420$ nm)	20 min + 100 min	85%
WO <sub>3</sub> /g-C <sub>3</sub> N <sub>4</sub> /Bi <sub>2</sub> O <sub>3</sub>	1	300 W Xenon lamp ( $\lambda > 420$ nm)	60 min + 60 min	80.2%
WO <sub>3</sub> @g-C <sub>3</sub> N <sub>4</sub> @MWCNT	0.2	500 W halogen lamp ( $\lambda > 420$ nm)	20 min + 120 min	79.54%
Mo/Nv-TCN	1	300 W Xenon lamp ( $\lambda > 420$ nm)	60 min + 60 min	94.45%

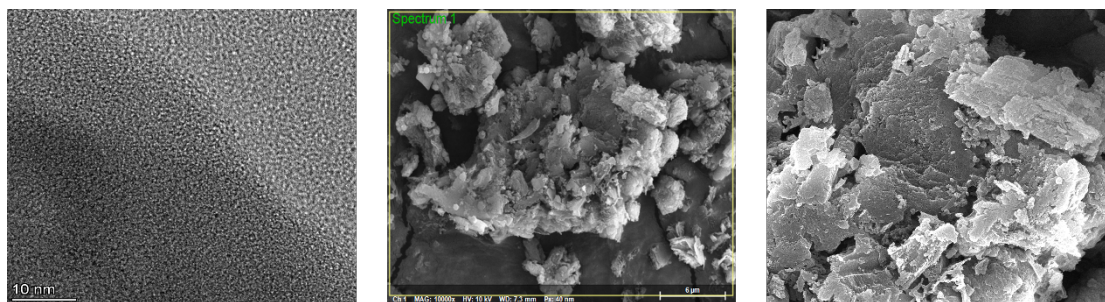


Fig. S1 TEM and SEM of 1.0GdCN.

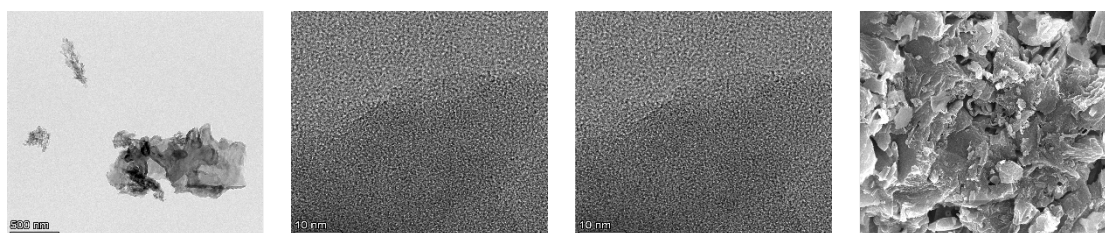


Fig. S2 TEM and SEM of CN.

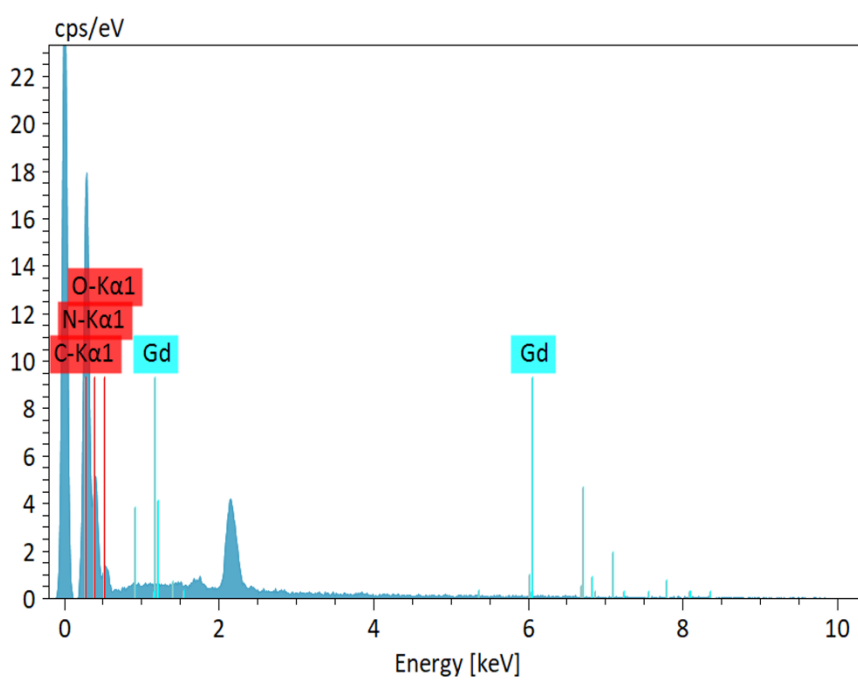


Fig. S3 Element content of 1.0GdCN.

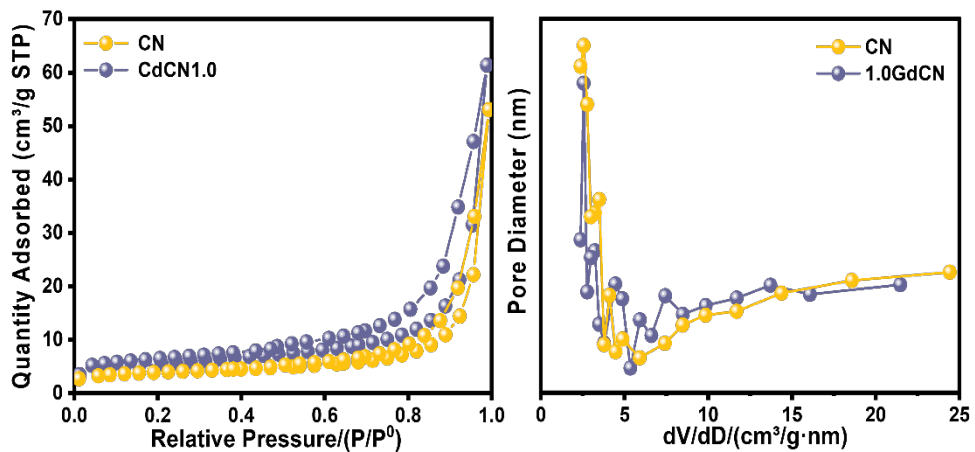


Fig. S4 Nitrogen adsorption-desorption isotherms (left) and the pore size distribution curves (right).

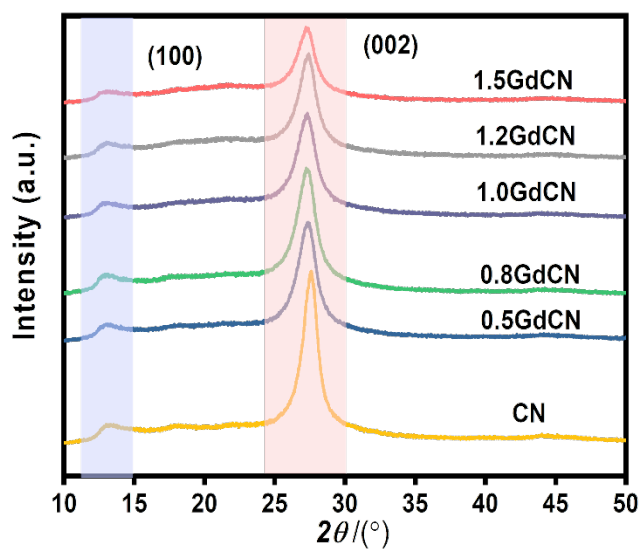


Fig. S5 XRD of CN, 0.5GdCN, 0.8GdCN, 1.0GdCN, 1.2GdCN and 1.5GdCN.



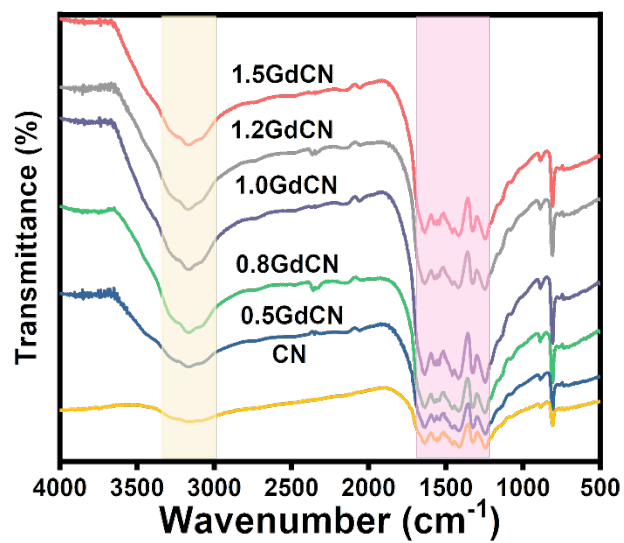


Fig. S6 FT-IR of CN, 0.5GdCN, 0.8GdCN, 1.0GdCN, 1.2GdCN and 1.5GdCN.

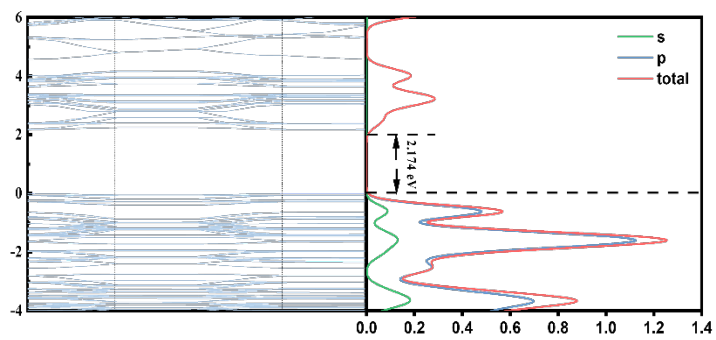


Fig. S7 DOS of CN.

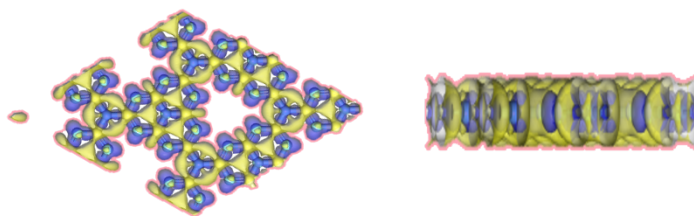


Fig. S8 differential charge of CN.

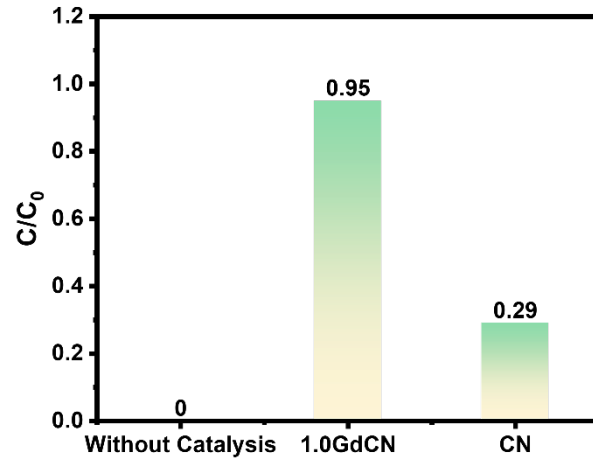


Fig. S9 Illumination comparison without photocatalyst.

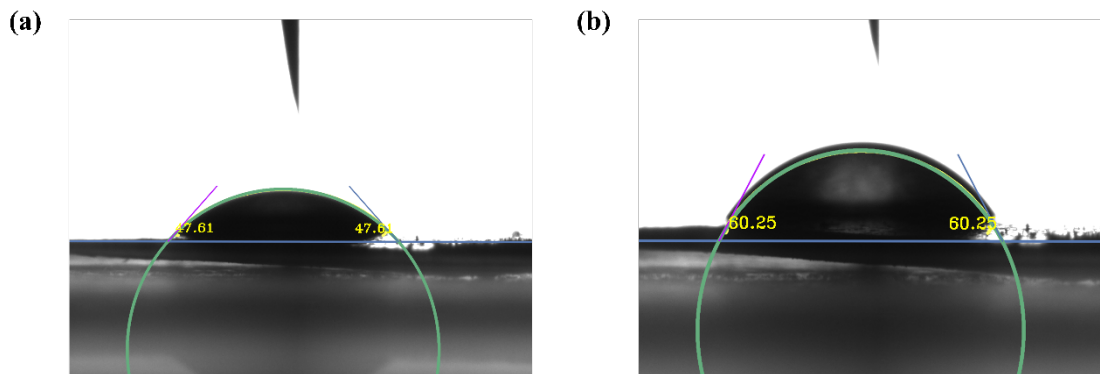


Fig. S10 Determination of hydrophilicity by 1.0GdCN (a) and CN (b).

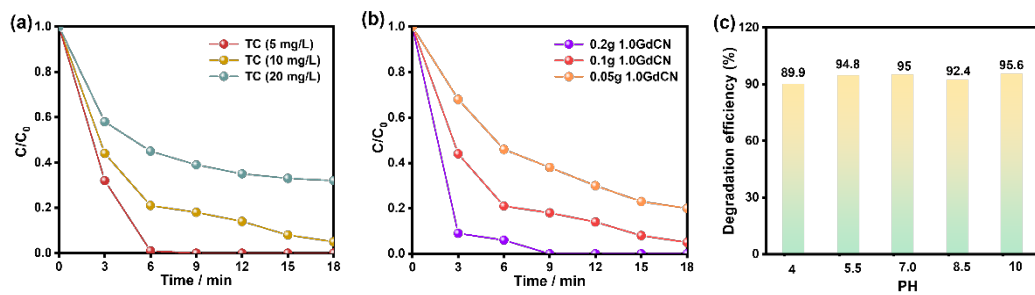


Fig. S11 Photocatalytic degradation of TC with different concentrations (a) and photocatalytic degradation of TC with different amounts of photocatalyst (b); The TC eradication efficiency of 1.0GdCN cloth at various pH (c).

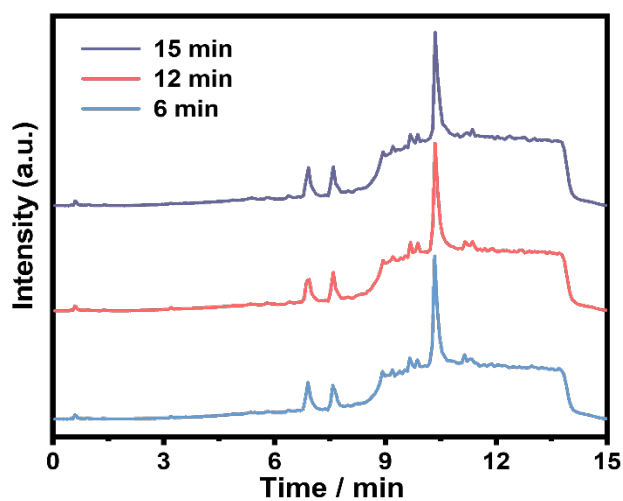


Fig. S12 Liquid chromatographic peaks at different times of 1.0GdCN.

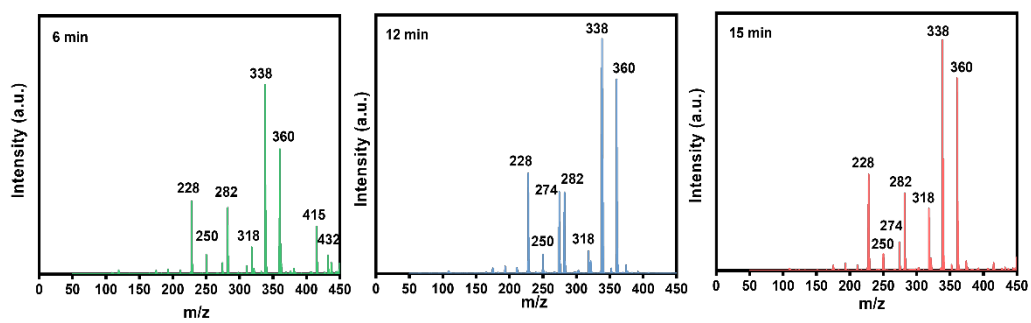


Fig. S13 Intermediate products of descending TC in different time and 6 min; 12 min; 15 min.

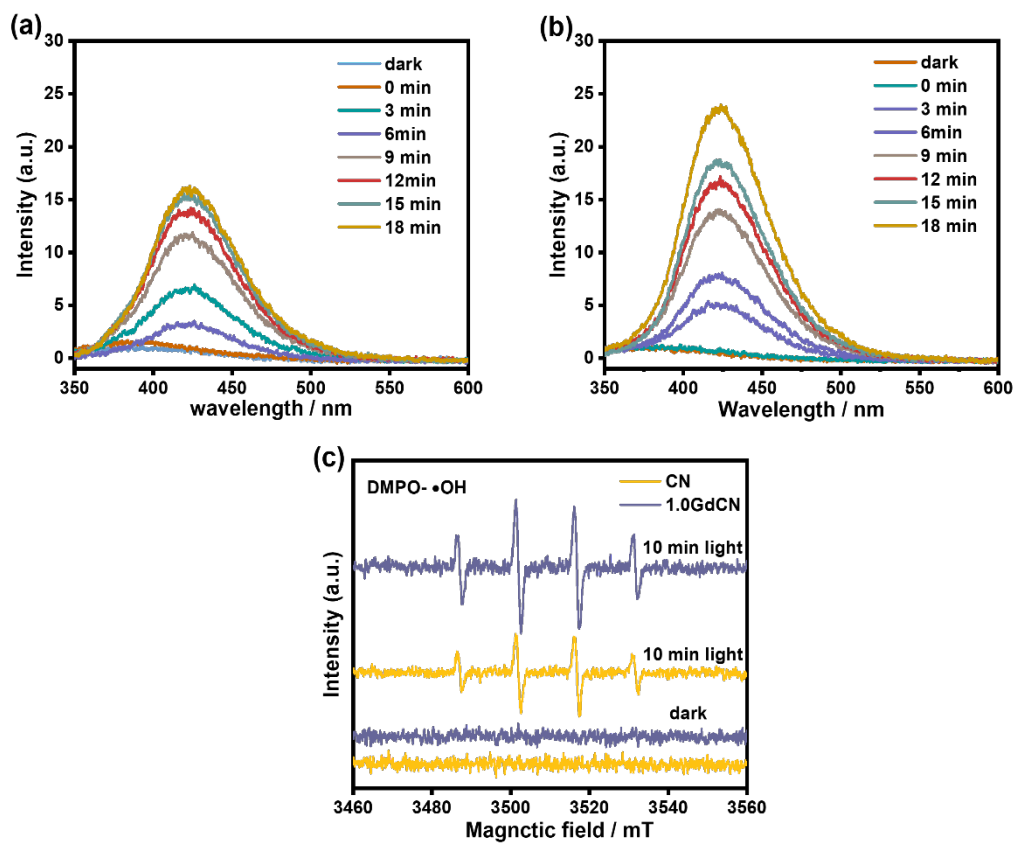


Fig. S14 Production of hydroxyl radical of (a) CN; (b) 1.0GdCN;  $\text{DMPO}\cdot\text{OH}$  of 1.0GdCN and CN.

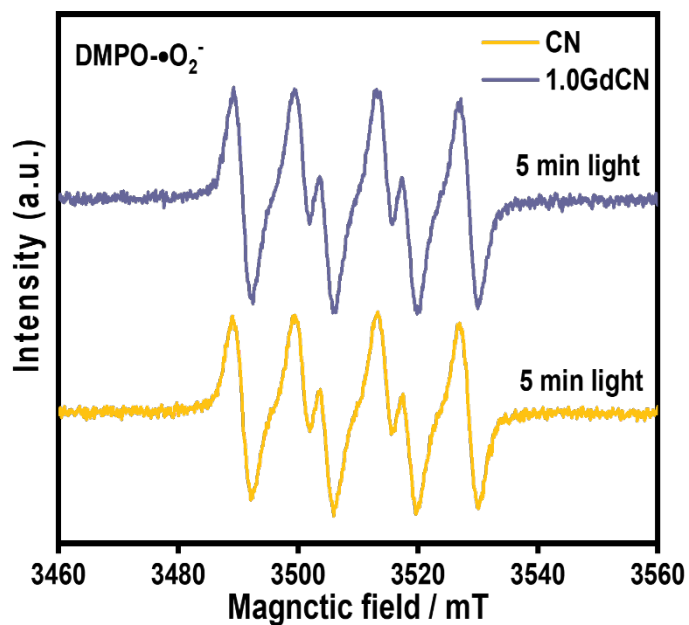


Fig. S15  $\text{DMPO}\cdot\text{O}_2^-$  of 1.0GdCN and CN.